Slip rates and locking depth variation along central and easternmost segments of North Anatolian Fault

B. Aktug, A. Dogru, H. Ozener, Michel Peyret

Geophysical Journal International

Geophys. J. Int. (2015) **202,** 2133–2149
GJI Geodynamics and tectonics

doi: 10.1093/gji/ggv274

Slip rates and locking depth variation along central and easternmost segments of North Anatolian Fault

B. Aktuğ,[1] A. Doğru,[2] H. Özener[2] and M. Peyret[3]

[1] *Department of Geophysical Engineering, Ankara University,* 06100 *Tandogan, Ankara, Turkey. E-mail: aktug@ankara.edu.tr*
[2] *Geodesy Department, Kandilli Observatory and Earthquake Research Institute, Bogazici University,* 34684 *Cengelkoy, Istanbul, Turkey*
[3] *Geosciences Montpellier, CNRS UMR-5243, F-34095 Montpellier, France*

Accepted 2015 June 23. Received 2015 June 23; in original form 2014 May 12

SUMMARY

While the kinematics of Anatolia plate and the North Anatolian Fault System (NAFS) has been studied extensively, the slip rate and locking depth along the NAFS are usually assumed constant in the analyses due to the lack of sufficient data. This is also partly due to the reasonably good fit of Euler small circle and partly due to the lack of spatial resolution of observations to determine slip rates independently from locking depths. On the other hand, recent geodetic studies show a contrast for locking depth between Marmara and other parts of the NAFS, implying a non-uniform locking depth across the NAFS. In this study, we analyse new GPS data and homogenously combine available data sets covering the eastern part of the NAFS to form the most complete data set. In particular, we incorporate the first results of Turkish Real-Time Kinematic GPS Network (CORS-TR) into our data set. A detailed analysis of three profiles within the NAFS reveals an increase of locking depth in the middle profile to 19.1 ± 3.4 km from 11.9 ± 3.5 km in the easternmost profile while the slip rate is nearly constant (20–22 mm yr^{-1}), which implies a variation of strain rate of ∼100 nanostrain yr^{-1}. Assuming a constant locking depth throughout whole NAFS gives an average locking depth of 14.3 ± 1.7 km. Our best estimates of slip rates in block modelling which takes the variation of locking depths into account are in the range between 22.5 and 22.8 mm yr^{-1} over eastern part of the NAFS.

Key words: Satellite geodesy; Space geodetic surveys; Continental neotectonics; Continental tectonics: strike-slip and transform; High strain deformation zones.

INTRODUCTION

North Anatolian Fault System (NAFS) is a ∼1500 km long strike-slip fault system delineating the boundary between Eurasia and Anatolia plates (Barka & Kadinsky-Cade 1988). The slip rates of the NAFS have been studied at various scales by GPS and InSAR (Straub *et al.* 1997; McClusky *et al.* 2000; Wright *et al.* 2001; Reilinger *et al.* 2006; Walters *et al.* 2011; Yavaşoğlu *et al.* 2011; Tatar *et al.* 2012; Cakır *et al.* 2012; Aktuğ *et al.* 2013a,b; Özener *et al.* 2013; Peyret *et al.* 2013; Cakir *et al.* 2014; Walters *et al.* 2014). GPS studies focusing on the general tectonic framework of Anatolia motion lack sufficient spatial resolution near individual segments of the NAFS and usually gives an upper bound for the slip rates of the NAFS (McClusky *et al.* 2000; Reilinger *et al.* 2006; Aktuğ *et al.* 2013a). The slip rates in those studies were obtained by differencing the rigid motion of the bounding plates with or without taking the elastic strain accumulation into account. Such a methodology intrinsically assumes a uniform slip rate over whole NAFS or its individual segments. Recent regional studies with relatively dense GPS arrays show that the locking depth and slip rate vary significantly over the NAFS (Özener *et al.* 2010; Yavaşoğlu *et al.* 2011; Tatar *et al.* 2012).

In the westernmost part of the NAFS (Marmara region), Meade *et al.* (2002) showed that a very shallow locking depth (5–6 km) is necessary to account for low strain observed near Marmara. The middle part of the NAFS was analysed by Yavaşoğlu *et al.* (2011) and they found that locking depth in the middle segment (near Ladik) is 16 km. Reilinger *et al.* (2006) have reported slip rates of 25.3–25.8 mm yr^{-1} with uniform locking depths of 15 km for these segments. The westward decrease in locking depth from the middle segment of the NAFS (near Ladik) to Marmara has been attributed to the variation of thickness of the crust, rock type, geochemical composition and recent seismic activity by Tatar *et al.* (2012). Complete unlocking has been observed at İsmetpaşa (Kaneko *et al.* 2013; Özener *et al.* 2013) after 1944 Gerede Earthquake. Tatar *et al.* (2012) has found that the fault locking depth increases westwards from 8.1 ± 3.3 km in Erzincan up to 12.8 ± 3.9 km in Niksar. Similarly, Cakir *et al.* (2012) recently reported a creeping segment over 1999 İzmit earthquake rupture. The relatively shallower locking depth in the easternmost part of the NAFS could also be due to 1939 Erzincan

earthquake (Barka 1996). While 1992 Erzincan earthquake (Ms: 6.8) also occurred in the easternmost part, it is relatively limited in terms of magnitude and rupture length to have any permanent effect in the area.

Four InSAR studies have been available for the eastern NAFS. Wright *et al.* (2001) has analysed a 70 km long segment and found that InSAR results favours a slip rate of 17 to 32 mm yr^{-1} and a locking depth from 5 to 33 km. Their result corresponds to a locking depth of 18 ± 6 km if the slip rate is constrained to be 24 mm yr^{-1}. In a more recent work, Walters *et al.* (2011) has found that their InSAR analysis across the eastern NAFS (37.5°E–39.5°E) favours a slip rate of 20–26 mm yr^{-1} below a locking depth of 13.5–25 km. In very recent studies (not available at the time of submission of this paper), Cakir *et al.* (2014) reported a very shallow locking depth of 7 ± 2 km and a slip rate of 20 ± 3 mm yr^{-1} and Walters *et al.* (2014) presented revised estimates of slip rate and locking depth as 20 ± 3 mm yr^{-1} and 16 km for the eastern NAFS.

A reliable determination of the slip rates and the locking depths across the NAFS is important for understanding the strain accumulation. For a constant slip rate, doubling the locking depth results in halved strain rate over the fault surface but makes the deformation zone wider.

In this study, the variations of the slip rates and the locking depth were investigated through a rigorous combination of continuous and survey-mode GPS measurements. The locking depths for three individual profiles were robustly determined from a dense observation set and further employed in block modelling for uniform slip rates. A further attempt was made to determine the distributed back-slip. While our distributed back-slip cannot distinguish the individual patches at high resolution, it is still useful to show the relatively shallower locking depth in the eastern NAFS. The results also show that while the slip rates along all three segments are nearly at the same level and up to ∼20 km increase of the locking depth in the central part of the NAFS results in a strain rate decrease of ∼0.1 μstrain yr^{-1}, which could have further physical implications.

TECTONIC SETTING

The tectonics of Anatolian plate is governed by two main driving mechanisms: the push of Arabian plate in the east and the pull due to the subduction along Hellenic Arc in the SW (Dewey & Sengör 1979; Le Pichon & Angelier 1979; Jackson & McKenzie 1984). The NAFS delineates the northern boundary of Anatolian plate with Eurasia and is a dominantly strike-slip fault (Barka & Kadinsky-Cade 1988). The onset of the NAFS is considered to have started in the east 11–13 Ma ago (Şengör *et al.* 2005). However, several researchers suggested that the NAFS was formed in early Pliocene (∼5 Ma) (Barka & Kadinsky-Cade 1988; Bozkurt 2001). However, both the segmentation and the second-order fault structures in the region are still under dispute (Zabci *et al.* 2011; Erturaç & Tuysuz 2012; Koçbulut *et al.* 2014). Main tectonic features of Anatolia and surrounding regions are shown in Fig. 1.

While central Anatolia is often considered a quasi-rigid block with less than 50 nanostrain yr^{-1} internal deformation (Aktuğ *et al.* 2013a), western Anatolia is characterized by diffused deformation (Aktuğ *et al.* 2009a). However, recent geodetic studies reveal the gradual increase of velocities westward (Reilinger *et al.* 2006; Aktuğ *et al.* 2013a). Geological field observations and seismological evidence show that the deformation zone of the NAFS becomes larger to the west from ∼10 km in the east up to 200–300 km in the west (Şengör *et al.* 2005). Specifically, the segment between the Erzincan & Niksar has been reported to be as narrow as 10 km in the NAFS

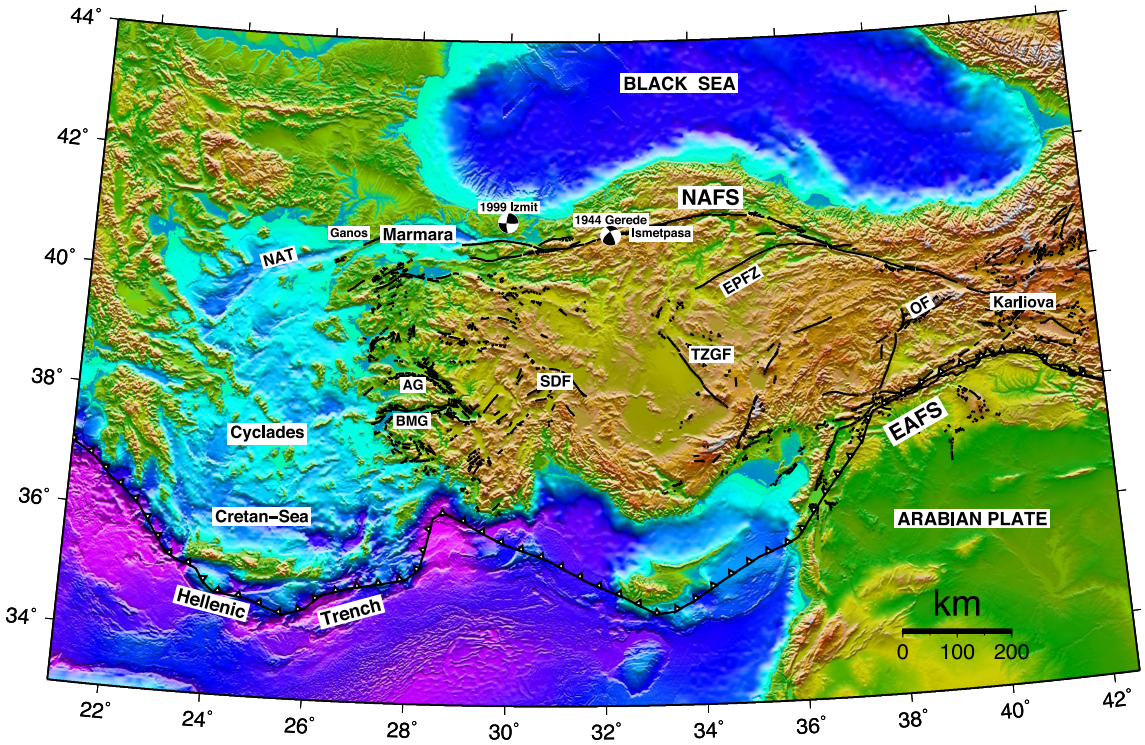

Figure 1. Tectonic framework and the main features in Anatolia and surrounding regions. NAFS: North Anatolian Fault System, EAFS: East Anatolian Fault System, OF: Ovacik Fault, NAT: North Aegean Through, SDF: Sultandağı Fault, EPFZ: Ezinepazarı Fault Zone, TZGF: Tuzgölü Fault, AG: Alaşehir Graben, BMG: Büyük Menderes Graben. Compiled and adapted from (Okay & Tüysüz 1999; Cambaz & Karabulut 2010). Topography and bathymetry are from ETOPO1.

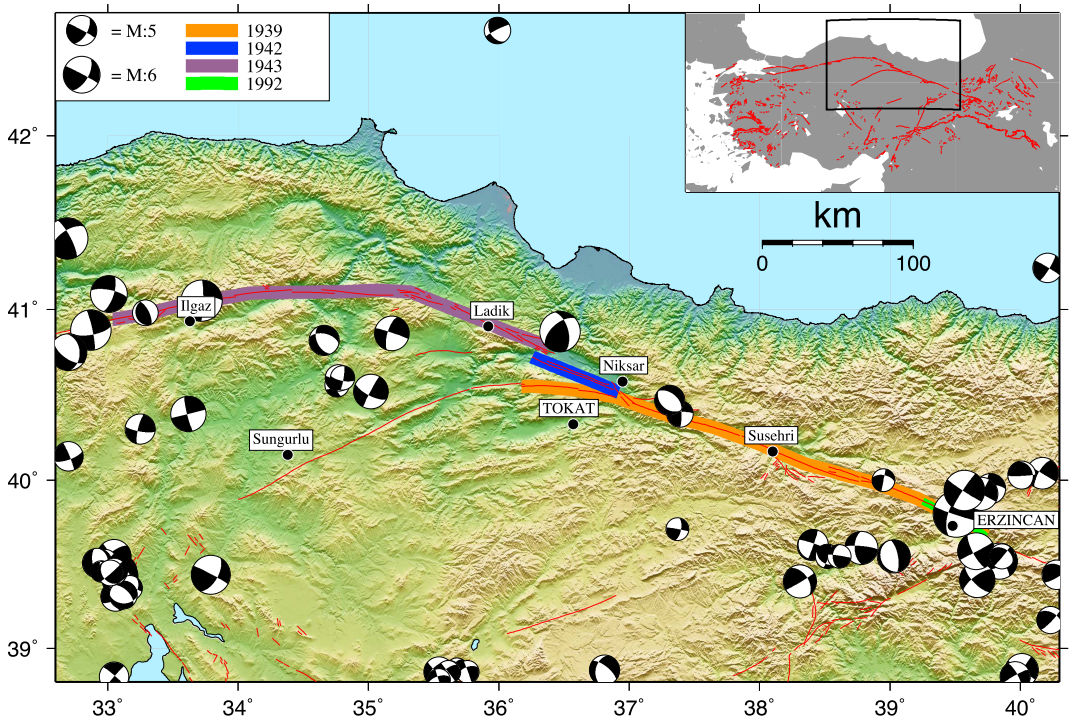

Figure 2. Study area and NAFS delineation. Active fault traces shown in red are from Şaroğlu *et al.* (1992) and the surface ruptures of 1939, 1942, 1943 and 1992 earthquakes are from Barka (1996). Focal mechanisms are from Kalafat *et al.* (2009) and cover the period between 1938 and 2008.

Atlas of Herece & Akay (2003). Similarly, paleomagnetic studies confirm a narrower shear zone in the east and much broader one in the west (Tatar *et al.* 1995).

The NAFS and the East Anatolia Fault System (EAFS) form a junction near Karliova (∼70 km east of Erzincan). The NAFS follows to the east and makes a bend in the central part (between Niksar and Ilgaz). The westernmost part of the NAFS forms a splay near Marmara Sea. The geological offsets of the NAFS segments have been studied at several time scales. Kozacı *et al.* (2007) has found a slip rate of 25.5 ± 9.5 mm yr^{-1} in the central part of the NAFS (41.0°N 33.7°E) with ^{36}Cl geochronology dating back to ∼2Ka. In another study, Kozacı *et al.* (2009) has found a slip rate of 18.6 ± 3.5 mm yr^{-1} still in the central part of the NAFS (41.1°N 35.0°E) with ^{10}Be geochronology dating back to ∼3Ka. Meghraoui *et al.* (2012) determined a slip rate of 17 ± 5 mm yr^{-1} at the westernmost part of the NAFS (Ganos). Hubert-Ferrari *et al.* (2002) has reported a Holocene slip rate of 18 ± 3.5 mm yr^{-1} and a Neogene slip rate of 6.5 mm yr^{-1}. In general, geological slip rates are up to 10 mm yr^{-1} lower than GPS estimates (McClusky *et al.* 2000; Reilinger *et al.* 2006; Aktuğ *et al.* 2013a).

Our study area comprises the central and eastern segments of the NAFS between the Ilgaz and Erzincan towns and hosted several large earthquakes (M > 7) during the last century (Barka 1996). The largest one is 1939 Erzincan (M:7.9) earthquake which ruptures the segments between Erzincan and Niksar and the splay between Niksar and Sungurlu (Fig. 2). Other notable earthquakes in the study area include 1942 Niksar-Erbaa (M:7.1) and 1943 Ladik (M:7.3) (Barka & Kadinsky-Cade 1988). While, the NAFS is predominantly a strike-slip fault, geological evidence suggest contraction and extension in the east and west of Ilgaz, respectively (Şengör *et al.* 2005). Recent geodetic studies reveal that the segment between Niksar and Sungurlu is not active (Aktuğ *et al.* 2013a). Ovacik Fault lying in the south of Erzincan has been analysed by Aktuğ *et al.* (2013b) and has been reported to have a left-lateral slip rate of 1.2 ± 0.3 mm yr^{-1}.

DATA AND ANALYSIS

GPS data and analysis

For the new data set, GPS observations for the years 1994, 1996, 1998 and 2004 were obtained from University NAVSTAR Consortium archive. The re-observations of the University NAVSTAR Consortium sites were carried out in 2007 by Kandilli Observatory and Earthquake Research Institute Geodesy Department. Each site was observed in two consecutive days with 10-h sessions using dual frequency GPS receivers in each campaign. GPS data reduction and estimation of velocity field was carried in a three step approach described by Dong *et al.* (1998). In the first step, the individual GPS campaign observations from 1994, 1996, 1998, 2004 and 2007 were processed as yearly solutions using GAMIT/GLOBK software (King *et al.* 2009). IGS final orbit products and IERS orientation products were incorporated into the analyses together with 18 IGS fiducial site observations. Normal equation matrix with loose constraints was produced for each yearly campaign. In the second step, taking loosely-constrained campaign solutions as quasi-observations, a combined normal equation matrix was obtained in a Kalman Filter scheme method using GLOBK software (King *et al.* 2009).

In the last step, the reference frames both coordinate and velocity estimates were defined by estimating 12-parameter transformation (3 translations, 3 rotations and their associated rates) to ITRF2008 coordinates of 14 selected IGS sites (BRUS, CAGL, GRAZ, JOZE, LAMA, MATE, NSSP, ONSA, POTS, SOFI, VILL, WTZR, ZIMM, ZWEN). The selection of sites for reference frame definition was made based on factors given in (Aktuğ *et al.* 2009b). Post-fit rms

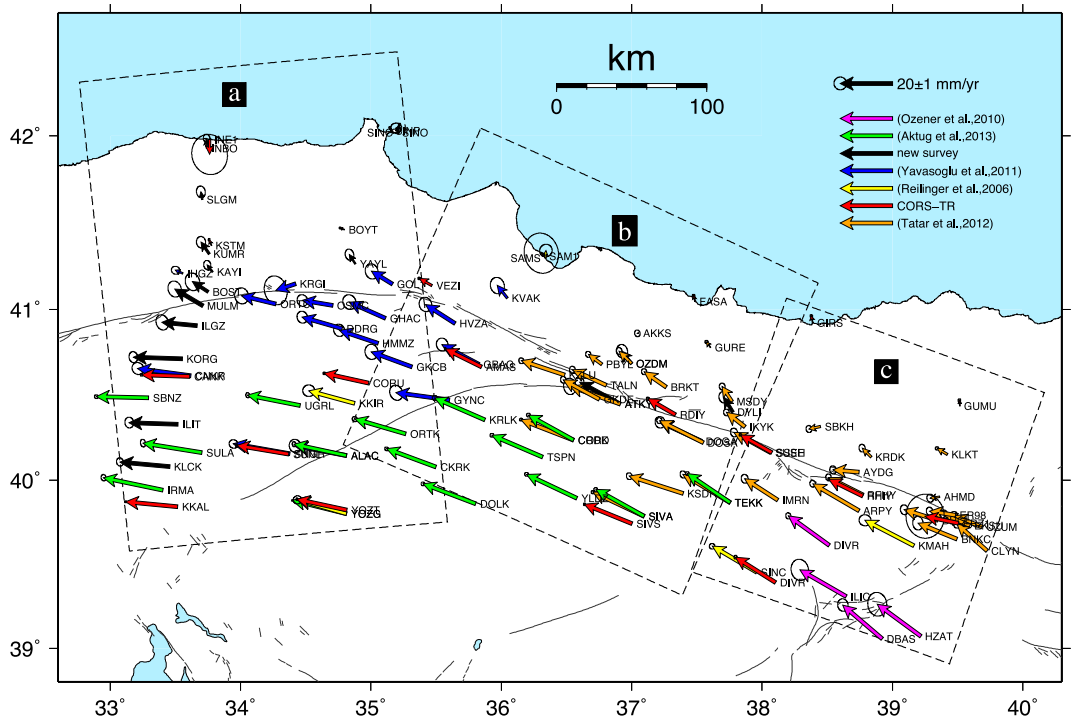

Figure 3. The individual velocity fields used in the analysis. The error ellipses of the velocity vectors are shown at 95 per cent confidence level. The boxes shown in dashed lines are the profiles used for the computation of the slip rates and the locking depth.

(root-mean-square) of 14 stations was found to be 0.79 mm and 0.34 mm yr^{-1} for coordinates and velocities, respectively.

Combined velocity field

In order to determine the slip rates reliably, the velocity fields published in previous studies were also incorporated to provide a denser velocity field. Tatar *et al.* (2012) provided a velocity in the eastern NAFS. While the velocity field given in (Reilinger *et al.* 2006) is highly sparse in the region, it still has several sites in the region. Aktuğ *et al.* (2013a) provided a dense velocity field covering the southern part of the NAFS's delineation limited to Central Anatolia. The velocity field published by Yavaşoğlu *et al.* (2011) covers the middle part of NAFS and serves to fill the gap between the eastern and western parts of the NAFS. Özener *et al.* (2010) provided a regional velocity field which complements the combined velocity field in the southeast. The GPS velocities given in (Tatar *et al.* 2012) were also included in the analysis. And, finally the velocities of continuous stations of CORS-TR network were incorporated (GCM 2013). Real Time Kinematic CORS-TR network covers a period of ∼5 yr since late 2008. After removing the annual and semiannual signals from the time series of the continuous stations, the 'real sigma' algorithm of (Herring 2003) was applied to account for the time-correlated noise on the velocity uncertainties of the continuous sites, following Reilinger *et al.* (2006) and He *et al.* (2013). The combined velocity field includes a total of 109 sites and the individual velocity solutions used for the combined velocity field are shown in Fig. 3. Due to the largest number of common sites pairwise with individual solutions, the Eurasia-fixed velocity field given in (Reilinger *et al.* 2006) was taken as the reference velocity field. The time series of several continuous stations were shown in Fig. 4. Following (Aktuğ *et al.* 2009a, 2013b) and Nocquet (2012), the velocity fields from different studies were transformed into the reference velocity frame given in (Reilinger *et al.* 2006) to remove any possible reference frame effect. The transformation model is

$$v_2 = v_1 + R(\Omega \times x), \tag{1}$$

where v_1 and v_2 are the velocity vectors in both local frames, R is the rotation matrix from Cartesian to local coordinate system, Ω is the Euler rotation vector, the '$\times$' stands for vector product and x is the position vector at each station. For each individual field, the reference variance factor was obtained by

$$\sigma_0^2 = \frac{r^T C r^{-1} r}{2n - 3}, \tag{2}$$

where r is the residual vector, C_r is the covariance matrix of observations and n is the number of sites used in the transformation such that the denominator in eq. (2) corresponds to the degree of freedom of the estimation. The reference variance factor of each individual transformation was used to scale the covariance matrix of the corresponding velocity field. Such a scaling of the original covariance matrix ensures that the reference variance factor to be 1. A similar methodology of combination was presented by Nocquet (2012), in which the individual transformation parameters were estimated in a single step rather than pairwise and then the variance factors for each solution was used to scale the individual solutions iteratively to make both the overall and the chi-square close to 1. The average fits of the individual velocity solution to the reference velocity solution are within the given uncertainties. The number of common sites, root mean square, the reference variance factor and the computed transformation parameters for each individual velocity field is given in Table 1. The final combined velocity field and the details about the observations are given in Table 2.

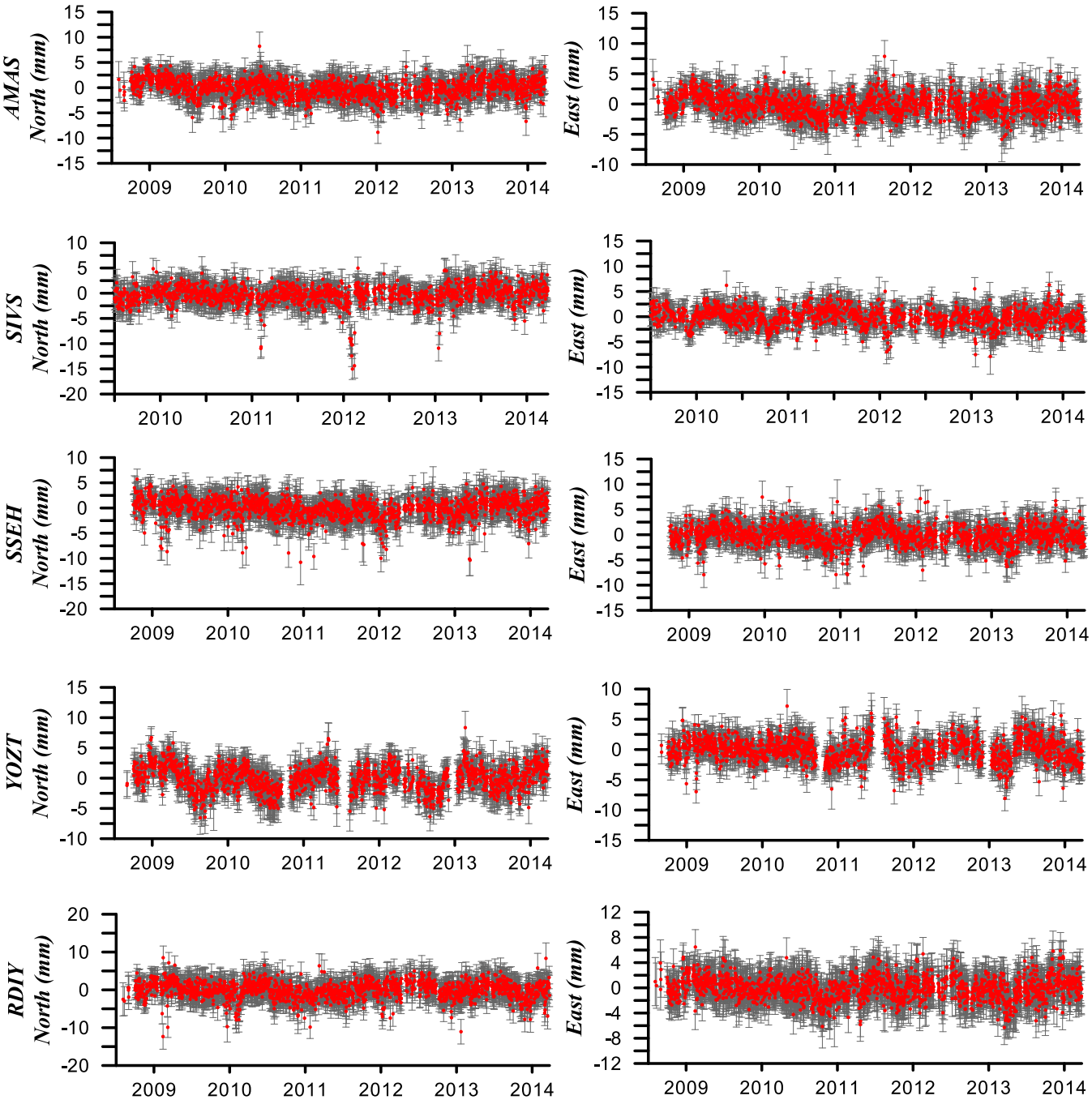

Figure 4. Detrended coordinate time-series examples of the continuous stations in ITRF2008 frame. The spatial distribution and the velocities of the continuous stations are shown in Fig. 3 (red arrows). The error bars are at 95 per cent confidence level.

Estimation of slip rate and locking depth

For an infinitely long vertical strike-slip fault, the classical relationship (Savage & Burford 1973) between the fault-parallel velocities and distance to the fault is given by

$$v = V_{\text{off}} + \frac{V}{\pi} \tan^{-1}\left(\frac{x + \Delta x}{D}\right), \tag{3}$$

where x is the perpendicular distance to the fault trace, V is the slip rate, D is the locking depth and v is observed fault parallel velocity, Δx is the fault offset and V_{off} is the velocity offset necessary to define velocities in the same velocity reference frame (Segall 2010). Δx was added to eq. (3) to compensate for any error resulting from simplification of fault delineation and to check any possible deviation from the assumed vertical fault geometry.

We used a robust Levenberg-Marquardt algorithm to simultaneously solve both the locking depth and slip rate along with other parameters given in eq. (3). The residuals were iteratively re-weighted and used to downweight the data points that are marked as outliers in the iteration to minimize their influence on the final estimates and to provide robust estimates (Seber & Wild 2003). The parameter estimates, the average mean squared error (mse) of the fit and the uncertainties of the estimates which were scaled by the square root of mse are given in Table 3. The locking depth and slip rate could be highly correlated depending on the network geometry. To assess the

Table 1. The rotation rates of individual solutions computed from the common sites to the reference velocity field (Reilinger *et al.* 2006). The individual data sets were transformed into the reference velocity frame using the computed rotation rates. The number of sites column (#) shows the total number of sites between each solution and the reference velocity field. ϕ, λ and Ω show the latitude, longitude and the rotation rate of the computed Euler poles. σ_o^2 is the reference variance factor computed from the residuals and used for scaling the covariance matrices of the individual solutions.

ϕ (°)	λ (°)	Ω (10^{-9} ° Myr^{-1})	# of sites	rms (mm yr^{-1})	σ_o^2	Source
−54.4009	9.4340	4.7	10	0.30	2.6	New survey
−47.4002	41.7292	27.77	3	1.27	4.6	(Özener *et al.* 2010)
−53.6579	1.5555	2.9	12	0.60	3.4	(Tatar *et al.* 2012)
67.3730	24.9637	0.7	20	0.57	1.3	(Yavaşoğlu *et al.* 2011)
54.0727	79.4485	39.5	17	0.55	6.7	CORS-TR
41.7674	15.0218	6.4	12	0.58	3.0	(Aktuğ *et al.* 2013a)
–	–	–	–	–	–	(Reilinger *et al.* 2006)[a]

[a]Reference velocity field.

sensitivity of the results with respect to the uncertainties of the velocities, we used a bootstrapping resampling approach to produce 300 data samples. These data samples were obtained by perturbing the original data set using the covariance structure of the original data set at 95 per cent confidence level. The results are shown in Fig. 5. While the correlation between the slip rate and locking depth is clear, they are well constrained by the data within their uncertainties as shown in Fig. 5. The velocity offset was also determined reliably within the uncertainty of the data uncertainty as clearly seen in Fig. 5, thus has no effect on the estimates.

Our bootstrap resampling results (Fig. 5) show that the increased locking depth in the western part (profile a) is sufficiently constrained by the density, distribution geometry and the precision of the velocity data. In particular, the velocity offset which could vary and be determined poorly in the case of lack of sufficient observations appears to be constrained within the level of submillimetre per year. While the correlation between the slip rates and the locking depths is clearly observed in Fig. 5, even the maximum variations appear to be constrained within 4 km and 2 mm yr^{-1} for the locking depth and the slip rate, respectively.

The results show that the slip rates across all segments (a through c) are statistically indistinguishable at a constant rate of ∼21 mm yr^{-1}. While the locking depth in the easternmost part of the NAFS is between 11.9 ± 3.5 and 12.6 ± 2.4 km, the middle part of NAFS has a relatively deeper locking depth (19.1 ± 3.4 km). The estimated fault offsets are below 1 km except for profile c but they are statistically insignificant in all three cases. The relatively higher fault offset in profile c could be related with the relatively high geometrical complexity of this segment (Cakir *et al.* 2014). The profiles showing the fit of the estimated parameters are shown in Fig. 6. Assuming a uniform locking depth and a slip rate along all three profiles gives an average value of slip rate 21.1 ± 0.8 mm yr^{-1} and an average locking depth of 14.3 ± 1.7 km. While the relatively shallower locking depths in the eastern segments of the NAFS show a localized strain distribution, a broader strain accumulation is observed in the middle part of the NAFS (Fig. 7).

Block modelling

After obtaining individual locking depths of profiles a–c, the slip rates were obtained through block modelling using ERBLOM (Elastic and Rigid BLOck Modeling) software given in Aktuğ *et al.* (2013a). The block modelling procedure consists of two distinct steps: application of the back-slip along block boundaries and estimation of block rotations. The rotations of two blocks separated by the NAFS were estimated while applying a uniform back-slip given in (Matsu'ura *et al.* 1986) to account for the elastic strain accumulation around fault zone. We followed a similar approach given in (McCaffrey 2002, 2005), where the block rotations are simultaneously estimated by minimizing the misfit of the velocities. The elastic strain accumulation was applied using the analytical equations given in Okada (1985). For the uniform back-slip, the locking depths of three block boundaries were taken as the estimated values of 19.1 ± 3.4, 12.6 ± 2.4 and 11.9 ± 3.5 km for profiles a-c, respectively. The weighted rms of the fit is 1.47 mm yr^{-1} for the data set employed. The residuals observed in the eastern part (∼39.7°E) lie within the deformation zone of Erzincan pull-apart basin. The same sites have similar residuals in the original paper (Tatar *et al.* 2012) probably due to non-elastic behaviour within high proximity to the fault zone and/or linear assumption of fault zone. The computed back-slips and residual velocity fields are shown in Fig. 8.

While the block model with a uniform back-slip is sufficient to quantify the strain accumulation across the NAFS, we further discretized the faults into 5 × 7 km patches to obtain distributed back-slips. Using the elastostatic green functions (G) which are linear with respect to the back-slip rates and by incorporating a finite-difference scheme Laplacian operator, the relation between the fault-parallel back-slip rates (v_{bs}) and the back-slip rates (s) at individual fault patches can be written as

$$\begin{bmatrix} v_{bs} \\ 0 \end{bmatrix} = \begin{bmatrix} G \\ \kappa L \end{bmatrix} [s], \tag{4}$$

where κ and L are the smoothing constant and the finite-difference approximation of the Laplacian operator, respectively. The Laplacian operator was used to constrain the rates of change of the back-slip rates along both the strike and the dip direction. To ensure that no reverse back-slip is obtained, the inversion was carried out by using a non-negative least-squares algorithm (Lawson & Hanson 1995). The balance between smoothing and misfit was realized through a smoothing constant which was determined empirically using a plot of solution roughness ($1/\kappa^2$) with respect to WRSS (Fig. 9). We used a roughness constant of 0.07 ($1/\kappa^2$). The distributed back-slip rates (Fig. 10) shows 15–20 mm yr^{-1} back-slip rates in the shallowest part (first 5 km) across whole fault line. However, the model resolution is not homogenous and only parts where sufficient data density is available near the fault have sufficient model resolution, such the those at 33.5°E, 37.0°E, 39°E and 39.5°E. While the shallow locking is clear in other parts, the near surface locking at 33°E, 34° and 36.5°E are not sufficiently resolved. Similarly, low back-slip rates are found between 5 km and 15 km depth for all segments except for the parts between 35°E and 35.5°E and between 37.5°E and

Table 2. The final velocity field used in the analysis and associated metadata. Type column refers to the type of observation with P (permanent) and S (survey mode). Continuous sites are CORS-TR sites. P-column shows in which profile the site is included as shown in Fig. 3. The survey-type measurements with epoch information are the new survey data and the sites compiled from literature are shown with the reference in the epoch columns.

Site	Lon. (°)	Lat. (°)	v_e (mm yr^{-1})	v_n (mm yr^{-1})	σ_{Ve} (mm yr^{-1})	σ_{Vn} (mm yr^{-1})	ρ_{VeVn}	P	Type	First Epoch	Last Epoch
AMAS	35.849	40.666	−13.9	6.9	0.2	0.2	−0.080	b	P	2008.59	2014.23
BOYT	34.797	41.461	−1.7	0.7	0.2	0.2	−0.035	a	P	2008.57	2014.23
CANK	33.610	40.609	−18.5	0.6	0.2	0.2	0.013	a	P	2008.58	2014.23
CORU	34.982	40.570	−17.0	3.8	0.2	0.2	−0.027	a	P	2008.58	2014.23
DIVR	38.104	39.394	−15.3	9.7	0.3	0.3	−0.019	c	P	2009.55	2014.23
ERZ1	39.506	39.746	−12.8	2.7	3.0	3.5	−0.009	c	P	2012.96	2014.23
FASA	37.485	41.046	−0.5	2.3	0.2	0.2	−0.040	b	P	2008.75	2014.23
GIRS	38.388	40.923	−0.5	2.6	0.2	0.2	−0.064	c	P	2008.66	2014.23
GUMU	39.516	40.437	−0.1	2.1	0.2	0.3	0.020	c	P	2008.61	2014.23
INE1	33.763	41.979	0.0	−5.7	2.8	3.2	−0.064	a	P	2012.77	2014.23
KKAL	33.518	39.843	−20.0	1.9	0.2	0.2	−0.028	a	P	2008.84	2014.23
KSTM	33.776	41.371	−0.8	2.1	0.2	0.2	−0.037	a	P	2008.61	2014.23
RDIY	37.336	40.385	−10.6	6.1	0.3	0.3	−0.030	b	P	2008.59	2014.23
RHIY	38.771	39.906	−13.0	6.4	0.2	0.2	−0.035	c	P	2008.66	2014.23
SAM1	36.334	41.309	−1.3	1.2	2.7	3.2	−0.078	b	P	2012.87	2014.23
SINP	35.154	42.030	−0.4	1.2	0.2	0.2	−0.017	a	P	2008.57	2014.23
SIVS	37.003	39.744	−18.3	7.4	0.2	0.2	−0.034	b	P	2008.57	2014.23
SSEH	38.075	40.163	−12.1	6.8	0.2	0.2	−0.042	c	P	2008.75	2014.23
SUNL	34.369	40.154	−19.9	3.3	0.2	0.3	−0.033	a	P	2008.58	2014.23
VEZI	35.467	41.138	−4.8	2.7	0.2	0.2	−0.080	b	P	2008.57	2014.23
YOZT	34.816	39.824	−19.2	4.1	0.2	0.2	−0.036	a	P	2008.67	2014.23
ATKY	36.912	40.447	−15.6	8.4	0.7	0.9	−0.090	b	S	2004.74	2007.64
BOST	33.751	41.101	−6.0	3.9	1.1	1.4	−0.120	a	S	2004.74	2007.64
DYLI	37.776	40.400	−3.5	5.7	0.7	0.9	−0.090	b	S	2004.74	2007.64
DOGA	37.535	40.229	−15.9	7.3	0.8	0.9	−0.070	b	S	2004.74	2007.64
ILGZ	33.668	40.905	−13.4	1.3	1.0	1.2	−0.160	a	S	2004.74	2007.64
ILIT	33.521	40.330	−18.7	0.6	0.7	0.8	−0.050	a	S	2004.74	2007.64
INBO	33.743	41.930	−0.1	3.7	0.5	0.7	−0.120	a	S	2004.74	2007.64
KAYI	33.786	41.217	−2.1	2.7	0.6	0.7	−0.110	a	S	2004.74	2007.64
KKIR	34.875	40.453	−17.6	4.8	0.9	0.9	−0.016	a	S	1994.73	2007.64
KLCK	33.457	40.081	−19.1	1.7	0.5	0.7	−0.100	a	S	2004.74	2007.64
KORG	33.553	40.713	−18.7	0.6	0.7	0.9	−0.090	a	S	2004.74	2007.64
OZDM	37.001	40.685	−3.7	4.7	0.9	1.0	−0.090	b	S	2004.74	2007.64
KUMR	33.759	41.322	−3.1	4.5	0.7	0.9	−0.050	a	S	2004.74	2007.64
MULM	33.711	41.021	−10.8	6.4	1.1	1.3	−0.130	a	S	2004.74	2007.64
SINO	35.205	42.020	0.7	3.1	0.2	0.2	0.000	a	S	1994.73	2007.64
SLGM	33.706	41.635	−0.5	2.9	0.7	0.9	−0.100	a	S	2004.74	2007.64
YAYL	34.881	41.264	−2.3	3.5	0.7	0.9	−0.140	a	S	2004.74	2007.64
ALAC	34.814	40.145	−20.2	4.4	0.3	0.4	−0.139	a	S	(Aktuğ *et al.* 2013a)	
CKRK	35.498	40.077	−18.9	7.0	0.3	0.3	−0.140	a,b	S	(Aktuğ *et al.* 2013a)	
CORD	36.554	40.237	−17.3	9.6	0.3	0.3	−0.032	b	S	(Aktuğ *et al.* 2013a)	
DOLK	35.803	39.860	−20.2	7.7	0.3	0.3	−0.077	b	S	(Aktuğ *et al.* 2013a)	
IRMA	33.405	39.942	−22.8	4.7	0.4	0.5	−0.115	a	S	(Aktuğ *et al.* 2013a)	
KRLK	35.875	40.355	−19.3	8.4	0.4	0.4	−0.099	b	S	(Aktuğ *et al.* 2013a)	
ORTK	35.267	40.272	−19.6	5.7	0.4	0.4	−0.100	a,b	S	(Aktuğ *et al.* 2013a)	
SBNZ	33.294	40.484	−20.0	0.4	0.3	0.3	−0.072	a	S	(Aktuğ *et al.* 2013a)	
SIVA	37.095	39.786	−18.5	10.3	0.3	0.3	−0.069	b	S	(Aktuğ *et al.* 2013a)	
SULA	33.703	40.163	−22.6	3.6	0.4	0.6	−0.182	a	S	(Aktuğ *et al.* 2013a)	
TEKK	37.757	39.867	−16.5	11.2	0.3	0.3	−0.079	c	S	(Aktuğ *et al.* 2013a)	
TSPN	36.318	40.136	−19.5	8.4	0.3	0.3	−0.065	b	S	(Aktuğ *et al.* 2013a)	
UGRL	34.458	40.439	−20.1	4.0	0.3	0.4	−0.096	a	S	(Aktuğ *et al.* 2013a)	
YLDZ	36.580	39.894	−19.3	9.2	0.3	0.3	−0.073	b	S	(Aktuğ *et al.* 2013a)	
YOZG	34.813	39.801	−20.8	5.2	0.1	0.1	−0.097	a	S	(Aktuğ *et al.* 2013a)	
DBAS	38.922	39.059	−15.1	12.9	0.8	1.0	−0.089	c	S	(Özener *et al.* 2010)	
DIVR	38.515	39.614	−15.7	11.3	0.4	0.5	−0.113	c	S	(Özener *et al.* 2010)	
HZAT	39.217	39.074	−16.7	12.2	1.5	1.9	−0.069	c	S	(Özener *et al.* 2010)	
ILIC	38.645	39.310	−17.8	10.2	1.4	1.7	−0.085	c	S	(Özener *et al.* 2010)	
KMAH	39.164	39.613	−18.7	9.7	0.9	0.9	−0.026	c	S	(Reilinger *et al.* 2006)	
SAMS	36.336	41.299	0.3	2.8	1.0	1.0	0.049	b	S	(Reilinger *et al.* 2006)	
SINC	37.958	39.454	−17.0	10.0	0.4	0.4	0.001	c	S	(Reilinger *et al.* 2006)	
SINO	35.205	42.020	−0.6	1.7	0.9	0.8	0.007	a	S	(Reilinger *et al.* 2006)	

Table 2. – (*Continued*)

Site	Lon. (°)	Lat. (°)	v_e (mm yr^{-1})	v_n (mm yr^{-1})	σ_{Ve} (mm yr^{-1})	σ_{Vn} (mm yr^{-1})	ρ_{VeVn}	P	Type	First Epoch	Last Epoch
YOZG	34.813	39.801	−18.8	5.4	0.7	0.6	0.005	a	S	(Reilinger *et al.* 2006)	
AHMD	39.361	39.902	−3.6	−0.5	0.5	0.6	−0.090	c	S	(Tatar *et al.* 2012)	
AKKS	37.054	40.863	−0.5	−0.1	0.4	0.5	−0.104	b	S	(Tatar *et al.* 2012)	
ARPY	38.743	39.820	−17.7	10.3	0.5	0.5	−0.082	c	S	(Tatar *et al.* 2012)	
ATKY	36.912	40.447	−19.3	6.8	1.0	1.3	−0.088	b	S	(Tatar *et al.* 2012)	
AYDG	38.743	40.047	−9.9	0.9	0.5	0.6	−0.088	c	S	(Tatar *et al.* 2012)	
BHCL	39.349	39.762	−12.9	4.1	0.6	0.8	−0.078	c	S	(Tatar *et al.* 2012)	
BNKC	39.494	39.652	−14.9	6.1	0.8	1.1	−0.055	c	S	(Tatar *et al.* 2012)	
BRKT	37.265	40.547	−8.5	5.9	0.4	0.5	−0.090	b	S	(Tatar *et al.* 2012)	
CLYN	39.725	39.582	−11.5	10.3	0.5	0.7	−0.084	c	S	(Tatar *et al.* 2012)	
CRDK	36.554	40.237	−20.1	7.8	0.3	0.2	−0.032	b	S	(Tatar *et al.* 2012)	
DOSA	37.549	40.221	−16.8	8.4	0.4	0.5	−0.085	b	S	(Tatar *et al.* 2012)	
EKSU	39.593	39.733	−9.9	4.1	0.6	0.7	−0.098	c	S	(Tatar *et al.* 2012)	
ER98	39.482	39.793	−9.9	1.5	0.5	0.6	−0.083	c	S	(Tatar *et al.* 2012)	
GKDE	36.752	40.476	−13.8	7.4	0.5	0.5	−0.097	b	S	(Tatar *et al.* 2012)	
GURE	37.604	40.778	−1.5	2.1	0.3	0.2	−0.027	b	S	(Tatar *et al.* 2012)	
IKYK	37.869	40.313	−7.1	5.6	0.5	0.5	−0.082	b,c	S	(Tatar *et al.* 2012)	
IMRN	38.121	39.882	−12.7	8.2	0.6	0.7	−0.108	c	S	(Tatar *et al.* 2012)	
KLKT	39.420	40.151	−3.9	2.3	0.3	0.3	−0.034	c	S	(Tatar *et al.* 2012)	
KRDK	38.836	40.136	−3.4	3.4	0.5	0.6	−0.092	c	S	(Tatar *et al.* 2012)	
KSDR	37.394	39.921	−20.6	6.7	0.5	0.5	−0.090	b	S	(Tatar *et al.* 2012)	
KZLU	36.485	40.617	−16.6	5.5	0.4	0.5	−0.095	b	S	(Tatar *et al.* 2012)	
MSDY	37.771	40.463	−3.8	5.7	0.5	0.5	−0.067	b	S	(Tatar *et al.* 2012)	
OZDM	37.001	40.685	−4.9	4.8	0.5	0.6	−0.088	b	S	(Tatar *et al.* 2012)	
PBYL	36.770	40.680	−5.2	3.8	0.4	0.5	−0.090	b	S	(Tatar *et al.* 2012)	
RFHY	38.774	39.914	−13.2	6.7	0.4	0.5	−0.081	c	S	(Tatar *et al.* 2012)	
SBKH	38.448	40.316	−4.4	−1.0	0.5	0.6	−0.087	c	S	(Tatar *et al.* 2012)	
SIVA	37.095	39.786	−19.7	9.3	0.3	0.2	−0.035	b	S	(Tatar *et al.* 2012)	
SUSE	38.067	40.162	−14.1	7.8	0.6	0.7	−0.102	c	S	(Tatar *et al.* 2012)	
TALN	36.804	40.557	−12.9	5.9	0.5	0.6	−0.103	b	S	(Tatar *et al.* 2012)	
TEKK	37.757	39.867	−18.2	10.8	0.5	0.6	−0.101	c	S	(Tatar *et al.* 2012)	
UZUM	39.688	39.724	−10.7	4.3	0.5	0.7	−0.083	c	S	(Tatar *et al.* 2012)	
ALAC	34.814	40.145	−19.8	3.7	0.9	1.0	−0.084	a	S	(Yavaşoğlu *et al.* 2011)	
CNKR	33.620	40.614	−20.4	2.7	0.9	0.9	−0.100	a	S	(Yavaşoğlu *et al.* 2011)	
DDRG	34.780	40.888	−15.3	4.4	0.8	0.9	−0.104	a	S	(Yavaşoğlu *et al.* 2011)	
GBAG	35.830	40.681	−14.2	7.5	0.9	1.0	−0.077	b	S	(Yavaşoğlu *et al.* 2011)	
GHAC	35.113	40.949	−13.9	6.2	1.0	1.2	−0.101	a	S	(Yavaşoğlu *et al.* 2011)	
GKCB	35.316	40.666	−15.6	5.7	1.0	1.2	−0.053	a,b	S	(Yavaşoğlu *et al.* 2011)	
GOL1	35.166	41.146	−8.0	4.9	1.0	1.2	−0.117	a	S	(Yavaşoğlu *et al.* 2011)	
GYNC	35.604	40.471	−20.5	2.8	1.0	1.2	−0.154	b	S	(Yavaşoğlu *et al.* 2011)	
HMMZ	35.054	40.802	−14.9	5.0	0.9	1.0	−0.088	a	S	(Yavaşoğlu *et al.* 2011)	
HVZA	35.645	40.919	−11.3	7.2	1.0	1.1	−0.105	b	S	(Yavaşoğlu *et al.* 2011)	
IHGZ	33.558	41.208	−2.8	1.3	0.7	0.6	−0.078	a	S	(Yavaşoğlu *et al.* 2011)	
KRGI	34.422	41.150	−7.6	−2.6	1.8	2.3	−0.141	a	S	(Yavaşoğlu *et al.* 2011)	
KVAK	36.046	41.065	−3.8	4.8	1.1	1.3	−0.097	b	S	(Yavaşoğlu *et al.* 2011)	
ORTC	34.272	41.031	−13.2	3.2	1.1	1.3	−0.084	a	S	(Yavaşoğlu *et al.* 2011)	
OSMC	34.707	41.022	−11.7	1.9	0.8	0.9	−0.087	a	S	(Yavaşoğlu *et al.* 2011)	
SNGR	34.379	40.155	−21.6	3.8	0.7	0.7	−0.094	a	S	(Yavaşoğlu *et al.* 2011)	

Table 3. The results of the simultaneous estimation of the profile parameters. D, V, V_{off} and Δx are the locking depth, slip rate, velocity offset and the fault offset defined in eq. (3) and their computed one-sigma uncertainties. The last row shows the combined case where a uniform locking depth and slip rate were assumed along all the three profiles. Last column corresponds to mean squared error variance.

Profile	D (km)	V (mm yr^{-1})	V_{off} (mm yr^{-1})	Δx (km)	MSE (mm^2 yr^{-2})
a	19.1 ± 3.4	21.5 ± 1.2	−9.5 ± 0.3	−0.9 ± 1.9	2.47
b	12.6 ± 2.4	21.4 ± 1.3	−10.7 ± 0.4	0.9 ± 1.9	2.82
c	11.9 ± 3.5	19.8 ± 2.3	−10.7 ± 0.8	2.0 ± 2.3	3.32
All	14.3 ± 1.7	21.1 ± 0.8	−10.1 ± 0.3	−0.3 ± 1.0	3.04

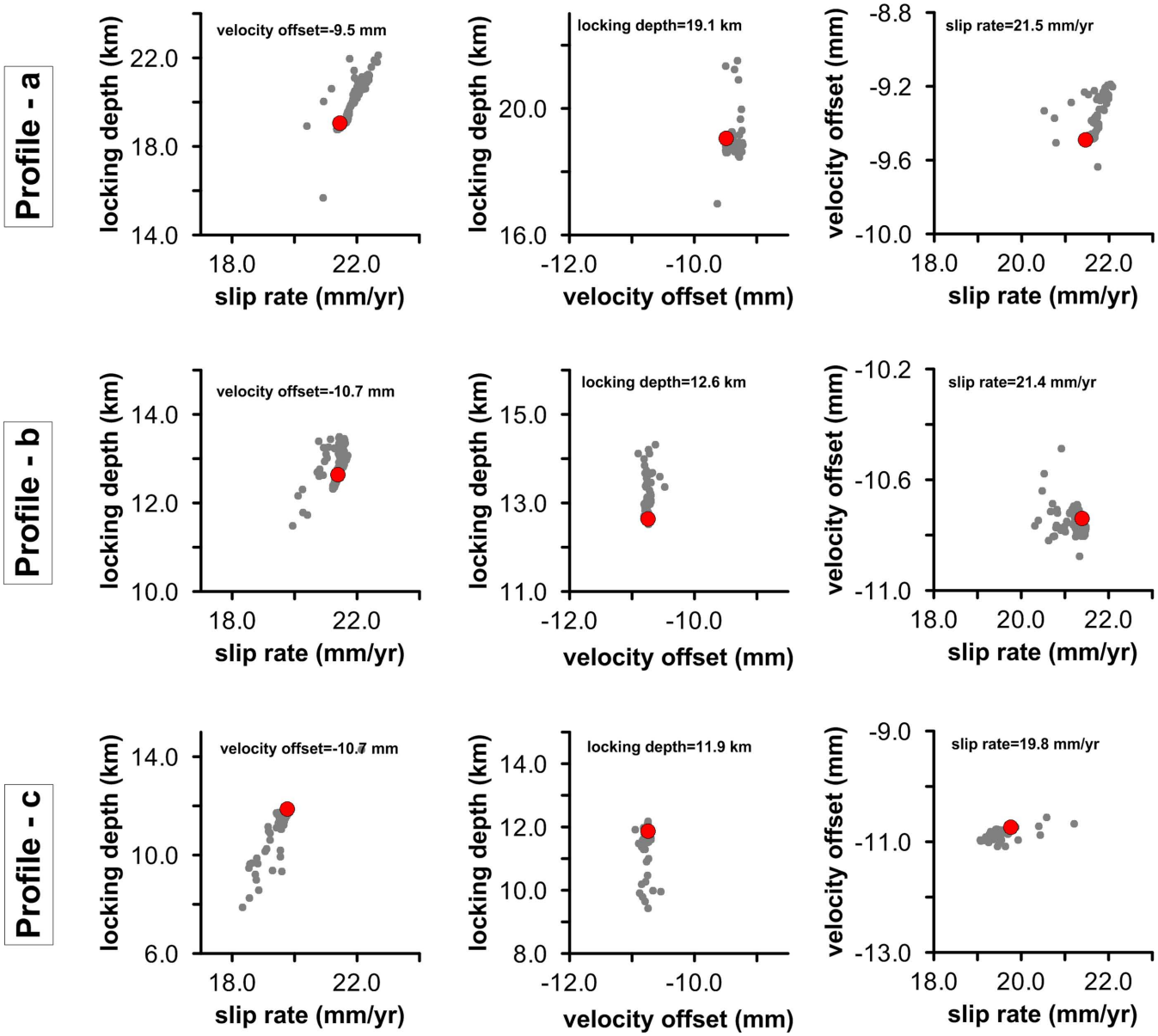

Figure 5. The bootstrap sensitivity analysis for the estimated parameters. The grey dots show the estimates from 300 bootstrap trials in which each velocity data set has the same covariance structure as the original covariance matrix of the observations. The velocity fields for the bootstrap trials were obtained via perturbing the original velocity data at 95 per cent confidence level by using the covariance matrix of the original observations. The red dots show the estimated values of the parameters from the original data set.

38°E. The signature of a local increase of locking depth between 34.5°E and 35°E in recent PS-InSAR results (Peyret *et al.* 2013) can also be observed in the distributed back-slip rates. Between 15 and 20 km depth, nearly all the segments have a moderate back-slip rate of ∼10 mm yr^{-1}.

DISCUSSION

Early studies about the determination of slip rate of the NAFS were based on the estimation of small circle using a set of GPS sites within rigid part of plate and extrapolating the rotation of plate along fault traces (Oral *et al.* 1995; Reilinger *et al.* 1997; McClusky *et al.* 2000). Such a methodology intrinsically involves the assumption of a constant rotation rate of Anatolia and constant slip rate across the NAFS. However, it has been shown that slip rates along a long fault system can vary depending on the fault orientations and elasticity variations even if the driving velocity is constant (Chéry 2008). Aktuğ *et al.* (2013a) showed that the westward increase of GPS velocities within Central Anatolia which has often been assumed rigid in many studies. In the estimation of the slip rates with so-called block models, in which the elastic strain accumulation is also taken into account along, the slip rates along the faults are estimated through differential rotation of bounding blocks (McCaffrey 2002, 2005). Such a modelling is also highly sensitive to block discretization, assumed locking depths and density of data. In particular, sufficient data are needed near block boundaries to distinguish non-rigid motion from rigid block rotation in the estimation procedure. Even if the slip rates are assumed constant across the whole NAFS, the accumulation and release of strain still depends on the variation of locking depth. In this respect, rigorous determination of slip rates and locking depths is also important for hazard studies.

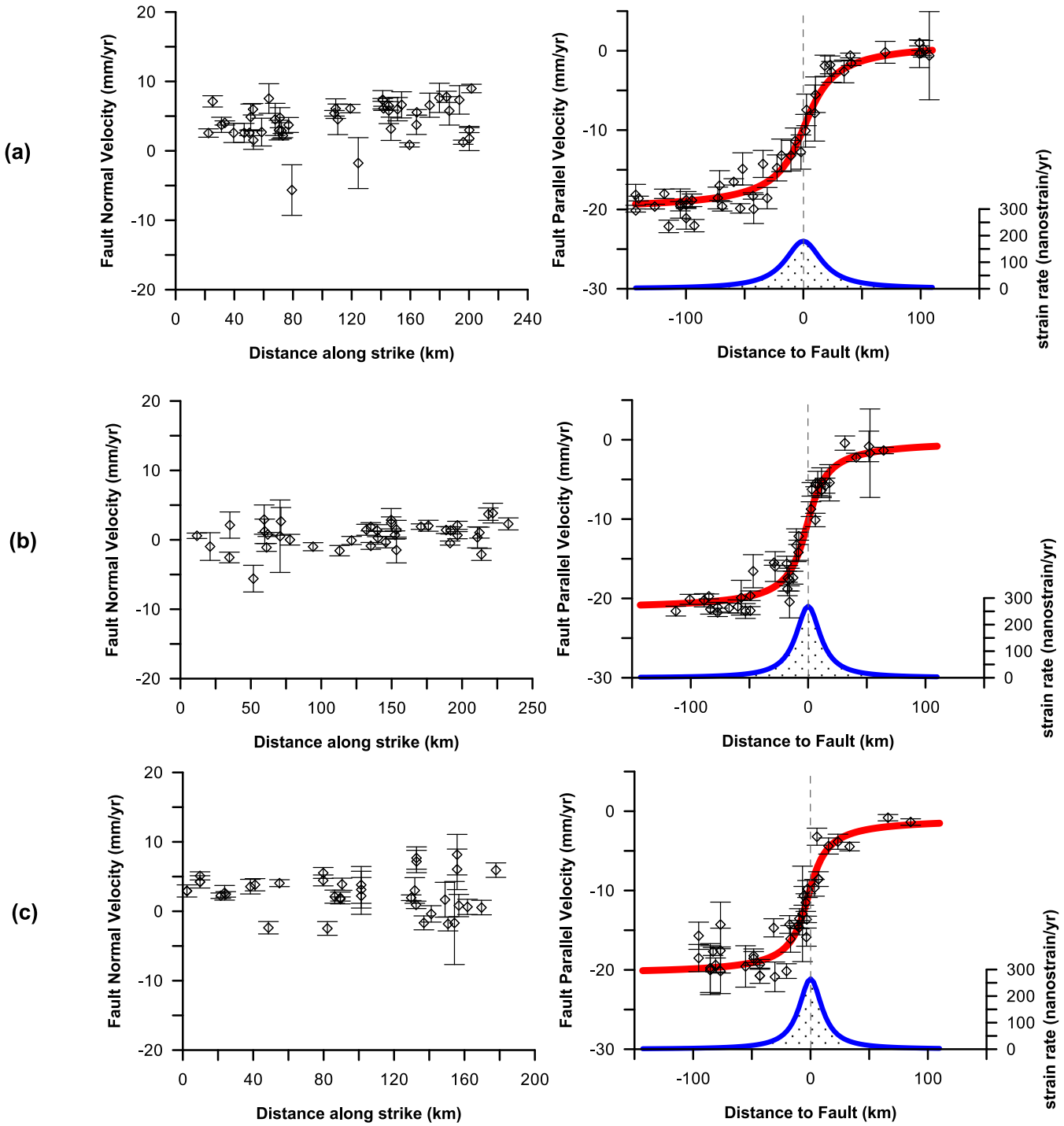

Figure 6. Along strike fault-normal velocities (left pane) and the observed and modelled fault-parallel velocities at the profiles 'a' to 'c' as shown in Fig. 3. The error bars of the observed velocities are at 95 per cent confidence level. The red and blue curves correspond to the fault-parallel profile of the modelled velocities and the spatial variation of the strain rates across the fault, respectively.

The central part of the NAFS (profile a) has been studied by Yavaşoğlu *et al.* (2011) and the slip rate reported ranges between 18.7 ± 1.6 and 21.5 ± 2.1 mm yr^{-1} assuming a locking depth of 16 km with uncertainty from 6 to 20 km. Our new survey data set which also includes that of (Yavaşoğlu *et al.* 2011) gives a best-fit slip rate of 22.5 ± 0.4 mm yr^{-1} and a locking depth of 19.1 ± 3.4 km. Considering the data density in this profile is about three times than those given in (Yavaşoğlu *et al.* 2011), the improvement in the uncertainty of slip rate is at the level expected. Similarly, Peyret *et al.* (2013) modelled permanent scatters of ERS and Envisat archives in the same region and found a slip rate of 20 mm yr^{-1} and a range for the locking depths as 15–20 km. They also reported a local increase of locking depth between E34°20′E and E34°50′. A similar pattern can also be observed in our distributed back-slip rates (Fig. 10). Reilinger *et al.* (2006) have reported right-lateral slip rates of 25.3–25.8 mm yr^{-1} with uniform locking depths of 15 km for these segments with extensional (i.e. fault normal slip in block modelling) rates of 8.0 ± 0.2 mm yr^{-1}. However, the density of

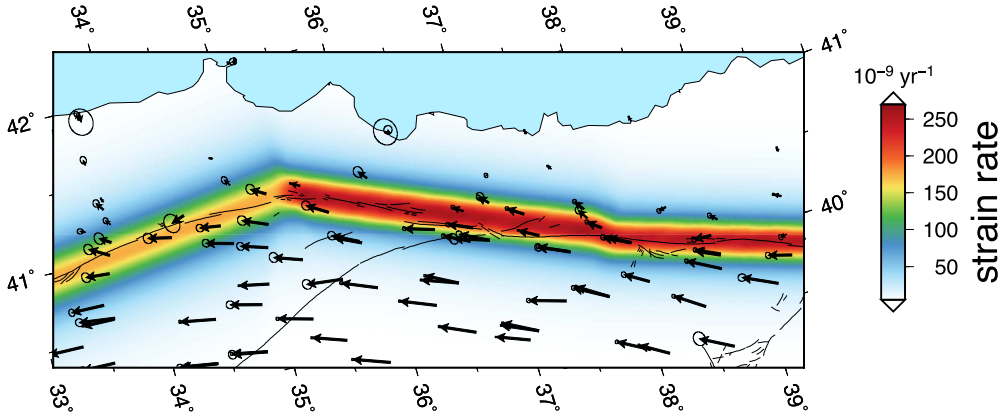

Figure 7. The variation and the extent of strain rates along the segments.

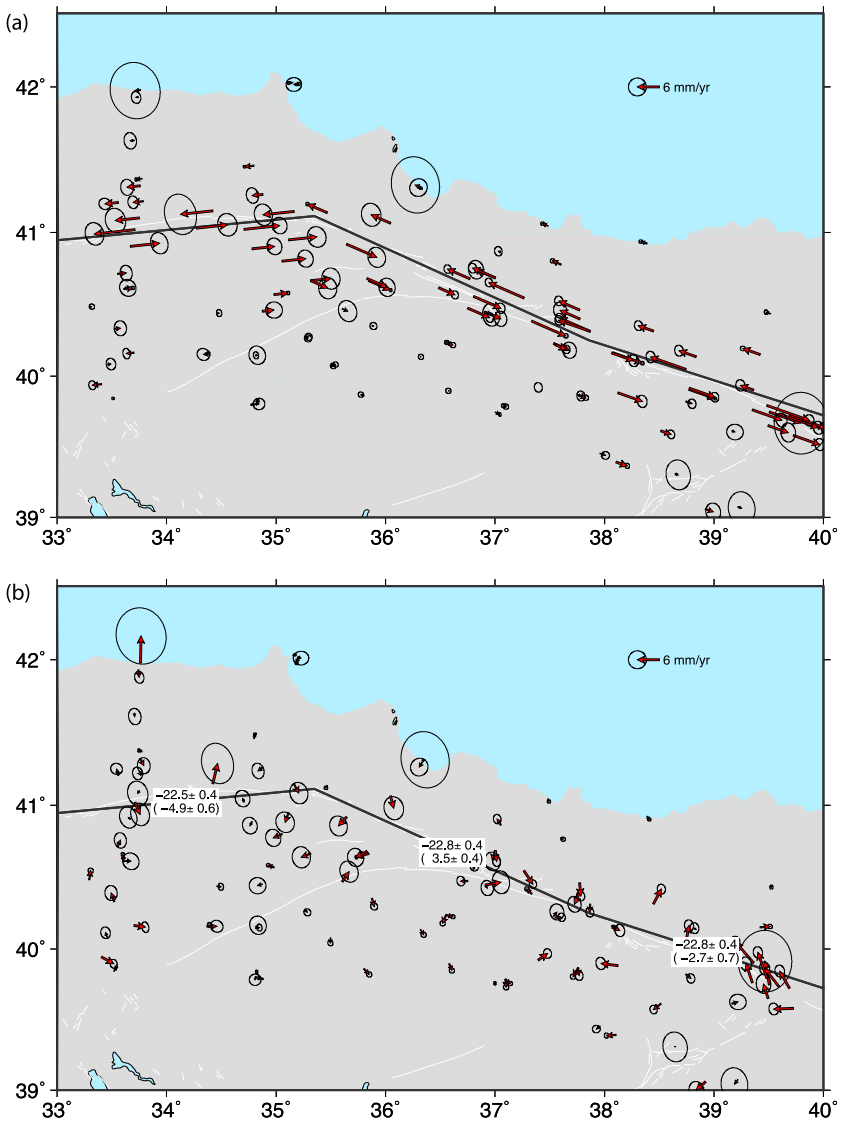

Figure 8. Block modelling results: (a) fault-parallel component of the back-slip and (b) the fault-parallel and fault-normal slip rates and the velocities residuals after block modelling. The upper and lower values at each segment show the fault-parallel and fault-normal slip rates, respectively. The negative values for the fault-parallel and fault-normal slip rates correspond to right lateral slip rates and contraction rates, respectively.

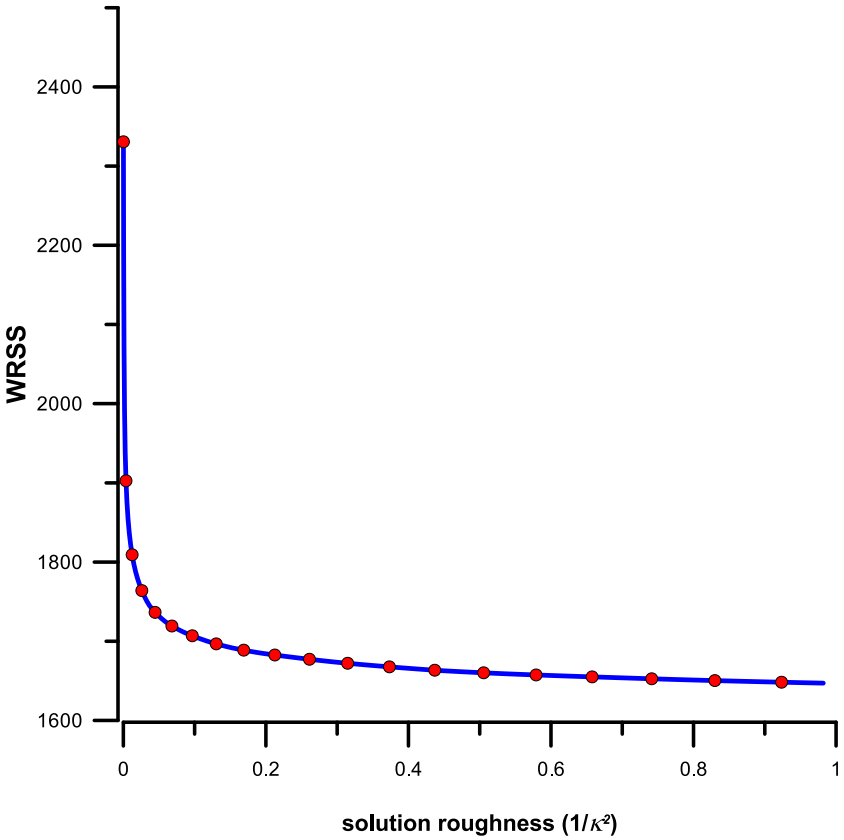

Figure 9. Solution roughness of the regularization versus the fit of the observations in the inversion.

their GPS data is too sparse in this region to identify the variations in the slip rates of individual segments. The obtained slip rate for the central segment of the NAFS is also comparable to the reported geological slip rates ranging between 20.5 ± 5.5 to 27 ± 7 mm yr^{-1} (Hubert-Ferrari *et al.* 2002; Hartleb *et al.* 2003; Kozacı *et al.* 2007). Our block model also gives a negative fault normal (contractional) slip rate of 4.9 ± 0.6 mm yr^{-1}, which is also expected considering the bending of the NAFS in the central segment. The estimates of slip rates and locking depths from various studies are shown in Figs 11 and 12, respectively.

The profiles (b and c) have been studied by Tatar *et al.* (2012) with GPS. They found that the fault locking depth increases westwards from 8.1 ± 3.3 in Erzincan up to 12.8 ± 3.9 km in Niksar. They also reported a westward increase of velocities from ∼16 to 24 mm yr^{-1}, which is also verified by large data set in (Aktuğ *et al.* 2013a). Reilinger *et al.* (2006) reported 25.8 ± 0.2 and 25.3 ± 0.2 mm yr^{-1} slip rates for profiles b and c, respectively. Wright *et al.* (2001) reported a slip rate of 17 to 32 mm yr^{-1} and a locking depth from 5 to 33 km for a 70 km long segment within the c profile. They also reported that assuming a locking depth of 18 km increases the slip rates up to 24 mm yr^{-1}. Walters *et al.* (2011) studied the same segment with InSAR and found that the easternmost part of the NAFS (37.5°E–39.5°E) favours a slip rate of 20–26 mm yr^{-1} below a locking depth of 13.5–25 km. We found a slip rate of 22.8 ± 0.4 mm yr^{-1} by using the block modelling approach and computed locking depths of 12.6 ± 2.4 km and 11.9 ± 3.5 km from the velocity profiles for profiles b and c, respectively. The computed slip rates from velocity profiles are also similar as 21.4 ± 1.3 mm yr^{-1} and 19.8 ± 2.3 mm yr^{-1} for profiles b and c, respectively. Since the employed blocks are much larger than the individual profile coverage, more observations were included to compute the slip rates in block modelling as reflected in their corresponding uncertainties. In that respect, our best-fit model of slip rate for the profiles b and c is 22.8 ± 0.4 mm yr^{-1} as computed from block modelling approach. Previous studies focusing on the entire NAFS show that the geological slip rates across the NAFS are lower than the GPS estimates in which the slip rate is estimated through large block rotations (Hubert-Ferrari *et al.* 2002; Reilinger *et al.* 2006; Aktuğ *et al.* 2013a). On the other hand, dense GPS observations across relatively small segments favours a slower slip rate (Yavaşoğlu *et al.* 2011; Tatar *et al.* 2012) which are closer to the geological estimates. This could be due to the rigid block and/or locking depth assumptions of former models.

The discrepancy between the results of various studies could be due to the trade-off usually not constrained with dense data network configuration. In regional modelling, estimating the slip rates assuming through block modelling could produce an upper bound depending on the chosen locking depth as revealed by the results of (Reilinger *et al.* 2006) or a local network as in the case of (Wright *et al.* 2001; Walters *et al.* 2011; Tatar *et al.* 2012). It is considered that the network configuration and data density given in this study provides the most reliable independent estimates of the variations in both the locking depth and slip rate.

In similar to the findings of Fialko (2006) for San Andreas Fault, we also investigated the asymmetry along all three segments. However, no statistically significant asymmetry was observed. To investigate a possible asymmetry, the eq. (3) was extended so as to

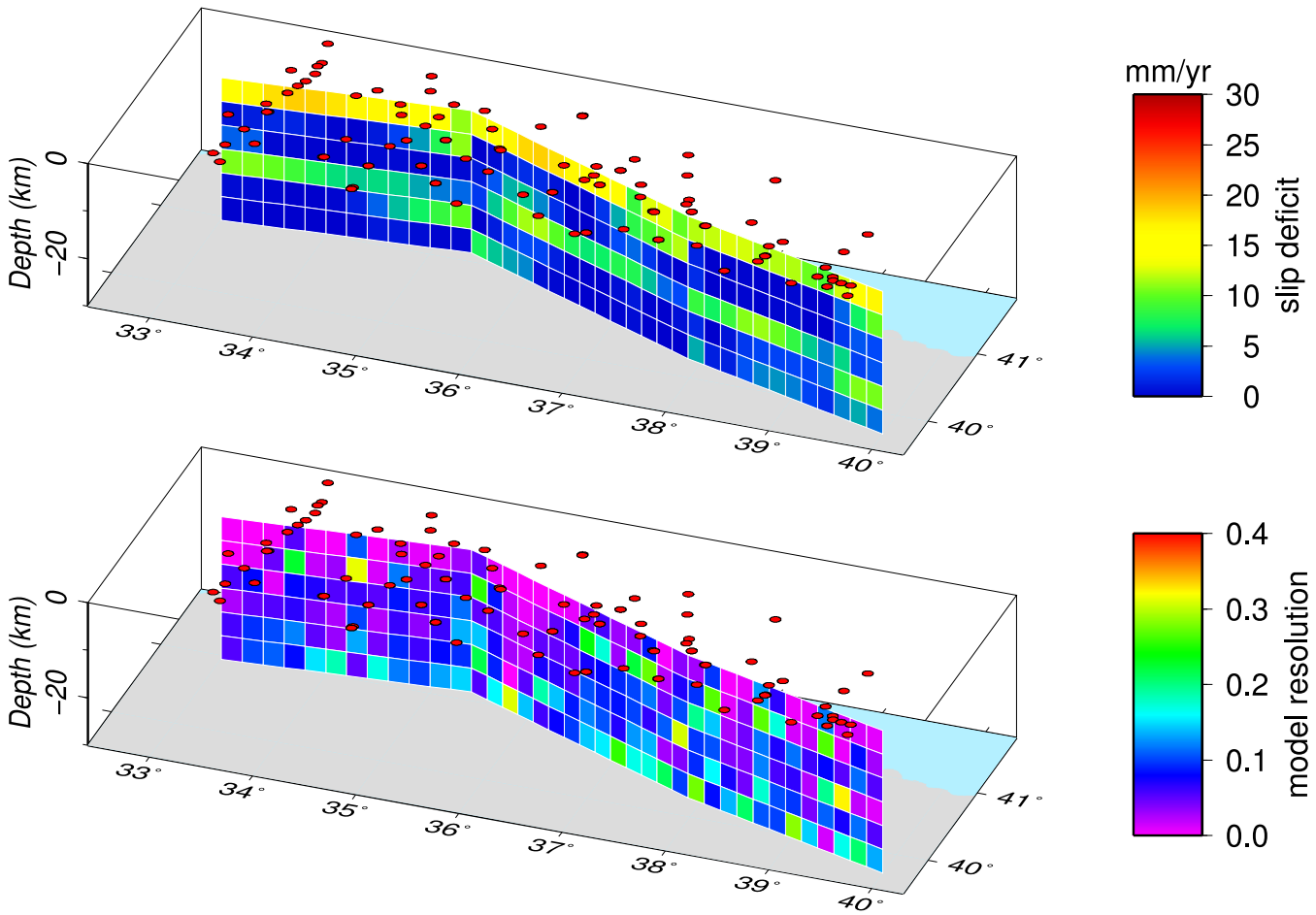

Figure 10. The distributed model of back-slip rates (upper) and the model resolution (lower). The red dot shows the distribution of the GPS sites on the surface. The patches have dimensions of 5 × 7 km. The models extend down to 30 km depth.

include an asymmetry term (K) as proposed by Le Pichon *et al.* (2005) and Jolivet *et al.* (2008)

$$v(x) = \begin{cases} \dfrac{2\,K\,V}{\pi} \tan^{-1}\left(\dfrac{x+\Delta x}{D}\right) & \text{if } x > \Delta x \\ \dfrac{2\,(1-K)\,V}{\pi} \tan^{-1}\left(\dfrac{x+\Delta x}{D}\right) & \text{if } x < \Delta x \end{cases}. \quad (5)$$

The fault offsets computed (Table 3) are all small and statistically insignificant. This result confirms the relatively simple linearity of the NAFS delineation although there are geological discontinuities and complexities. It also shows that NAFS is almost purely vertical in the studied region. The dipping of the fault would otherwise reveal itself as asymmetry in the profiles (Le Pichon *et al.* 2005; Fialko 2006; Jolivet *et al.* 2008).

The relatively shallower locking depth in the easternmost segment of the NAFS could be due to 1939 Erzincan earthquake (Barka 1996). While it is unclear, whether large earthquakes produce a decrease in locking depth, complete unlocking has been observed at Ismetpaşa (Kaneko *et al.* 2013; Özener *et al.* 2013) after 1944 Gerede Earthquake and at Izmit after 1999 İzmit earthquake rupture segment (Cakir *et al.* 2012). While complex frictional properties govern how the fault coupling evolves to a new state after a large earthquake (Scholz 1998), such a phenomenon could also be linked with the possibility of the post-seismic transient effect due to the 1939 Erzincan (M:7.9) earthquake, the largest 20th earthquake of the NAFS. The post-seismic studies for Izmit earthquake (Hearn *et al.* 2009; Wang *et al.* 2009) show that a power-law viscosity of the middle to lower crust is necessary to explain the observed post-seismic surface motion. Since the power-law rheology implies a lower viscous strength immediately after a large earthquake, which gradually becomes stronger with time by the releasing the post-seismic stress, the strength of the middle to lower crust with a power-law rheology would be weaker after an earthquake than it was before the earthquake. If the same power-law rheology is also valid for the eastern part of the NAFS, the total strength of the lithosphere could be weaker after the 1939 Erzincan earthquake than it was before. On the other hand, the depth given for Erzincan earthquake in earthquake catalogues is 20 km (Kalafat *et al.* 2011), which may not be constrained sufficiently by the available seismic network at that time.

The early estimates of the slip rates along the NAFS from sparse and large-scale geodetic networks monitoring are 24 ± 1 mm yr^{-1} (Oral *et al.* 1995; Reilinger *et al.* 1997; McClusky *et al.* 2000), significantly higher than the estimates of 18–21 mm yr^{-1} derived from paleoseismology for the Holocene period (Hubert-Ferrari *et al.* 2002; Kozacı *et al.* 2007; Kozacı *et al.* 2009). While recent localized InSAR and GPS studies which include dense profile data favour a lower slip rates and a closer estimate to the geological slip rates for the segment a (Yavaşoğlu *et al.* 2011; Peyret *et al.* 2013) and for the segments b and c (Tatar *et al.* 2012; Cakir *et al.* 2014; Walters *et al.* 2014), the estimates from large-scale sparse networks which utilize rigid block rotations for estimating the slip rates still show

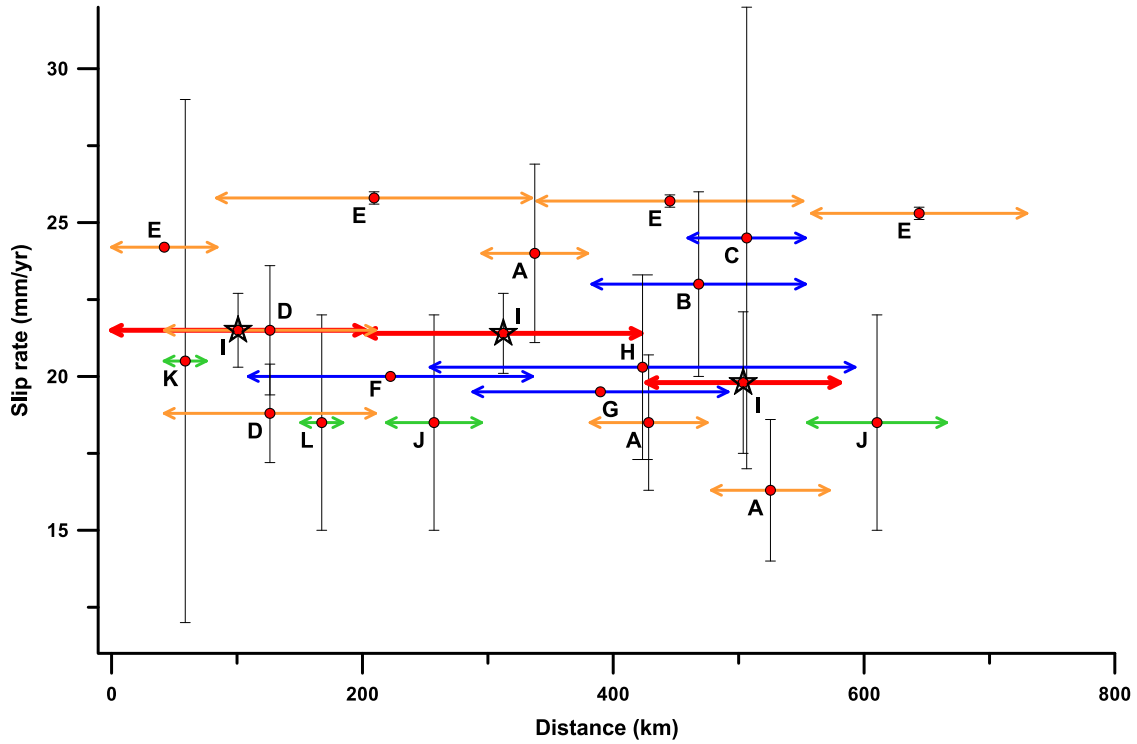

Figure 11. The variation of the slip rate along the eastern part of NAFS and the given uncertainties. The values are shown in red dots while the estimated values in this study are shown with an asterisk. The *x*-axis shows the distance from west to east and starts at 33° longitude. The uncertainties are shown at 1σ level. The estimates from GPS, InSAR and geology are shown in orange, blue and green lines, respectively. The estimates in this study are shown in red lines. (A) Tatar *et al.* (2012); (B) Walters *et al.* (2011); (C) Wright *et al.* (2001); (D) Yavaşoğlu *et al.* (2011); (E) Reilinger *et al.* (2006); (F) Peyret *et al.* (2013); (G) Cakir *et al.* (2014); (H) Walters *et al.* (2014); (I) this study; (J) Hubert-Ferrari *et al.* (2002); (K) Kozacı *et al.* (2007); (L) Kozacı *et al.* (2009).

higher slip rates 24–26 mm yr^{-1} (e.g. Reilinger *et al.* 2006). In this respect, it is considered that the most of the difference between GPS derived slip rates and the geological estimates in such studies should be associated with the resolution of the available geodetic network. Moreover, pure homogenous elastic models does not take the variation of the elasticity into account which could reveal itself as variation of the slip rate, locking depth and both (Chéry 2008). Our results, which provide the most complete GPS velocity in the area including the continuous stations for the first time, also confirm this hypothesis and provide slip rates consistent with the geological estimates within their uncertainties (Fig. 11).

The distributed back-slip rate model (Fig. 10) shows a higher rate of 15–20 mm yr^{-1} near surface (0–5 km) and a very low back-slip rates of 0–5 mm yr^{-1} immediately beneath (5–15 km). Relatively moderate back-slip rates of 5–10 mm yr^{-1} are observed at depth between 15 and 20 km. However, the obtained model resolution does not allow further investigation of the possible physical implications of such layering of the back-slip rates.

The latest large earthquake on the ruptures of 1942 (M_w:7.1) and 1943 (M_w:7.3) earthquakes (Fig. 2) is the 1668 earthquake between ~33°E and ~38°E (Ambraseys 1970; Ambraseys & Finkel 1988). 1668 earthquake also covers the western half of the 1939 (M_w:7.9) Erzincan earthquake. The latest large earthquake on the eastern half of the rupture of Erzincan earthquake is the 1254 earthquake, although the previous earthquakes (499 A.D., 717–844 A.D., 1045) on this segment show a nearly regular recurrence pattern of ~250 yr (Kozacı *et al.* 2011). Considering the elapsed times since the latest earthquakes until 1939 (since 1254) and until 1943 (since 1668) earthquakes, the relatively higher strain rate in the easternmost part of the NAFS and assuming a uniform shear modulus of 30 GPa, the difference in total accumulated stress between the eastern and middle segments is ~41 bars, consistent with the static stress drop difference of 44 bars computed from surface slip measurements (Barka 1996). However, static stress drop is highly sensitive parameter and values as low as 12 bars for the difference between the stress drops of 1939 and 1943 earthquakes has been estimated by elastic models (Stein *et al.* 1997).

CONCLUSION

The density and the distribution of the GPS networks seem to have an effect on the slip rates. In simultaneous estimation of the slip rates and locking depths using the profiles a–c, the slip rates were found to be 21.5 ± 1.2, 21.4 ± 1.3 and 19.8 ± 2.3 mm yr^{-1} for the segments a, b and c, respectively. Such nearly constant slip rates are consistent with the Holocene slip rates of 18–21 mm yr^{-1} (Hubert-Ferrari *et al.* 2002; Kozacı *et al.* 2007; Kozacı *et al.* 2009) as opposed to the previous estimates of 24 ± 1 mm yr^{-1}.

The relatively shallow locking depth in the easternmost part of the NAFS could be due to the post-seismic transient after 1939 Erzincan (M:7.9) earthquake. Since complete unlocking (creeping) phenomena after a large shock have been observed elsewhere on the NAFS (such as İsmetpaşa after 1944 Gerede earthquake and at near İzmit after 1999 İzmit earthquake), a partial unlocking at depth due to 1939 Erzincan earthquake could be responsible for the observed shallow locking depth.

The difference in strain rates between the rupture surface of 1939 Erzincan M:7.9 and 1943 Tosya earthquake (M:7.3) results in a total stress difference of 41 bars, when combined with the elapsed time between the 1939–1943 earthquakes and the previous events in

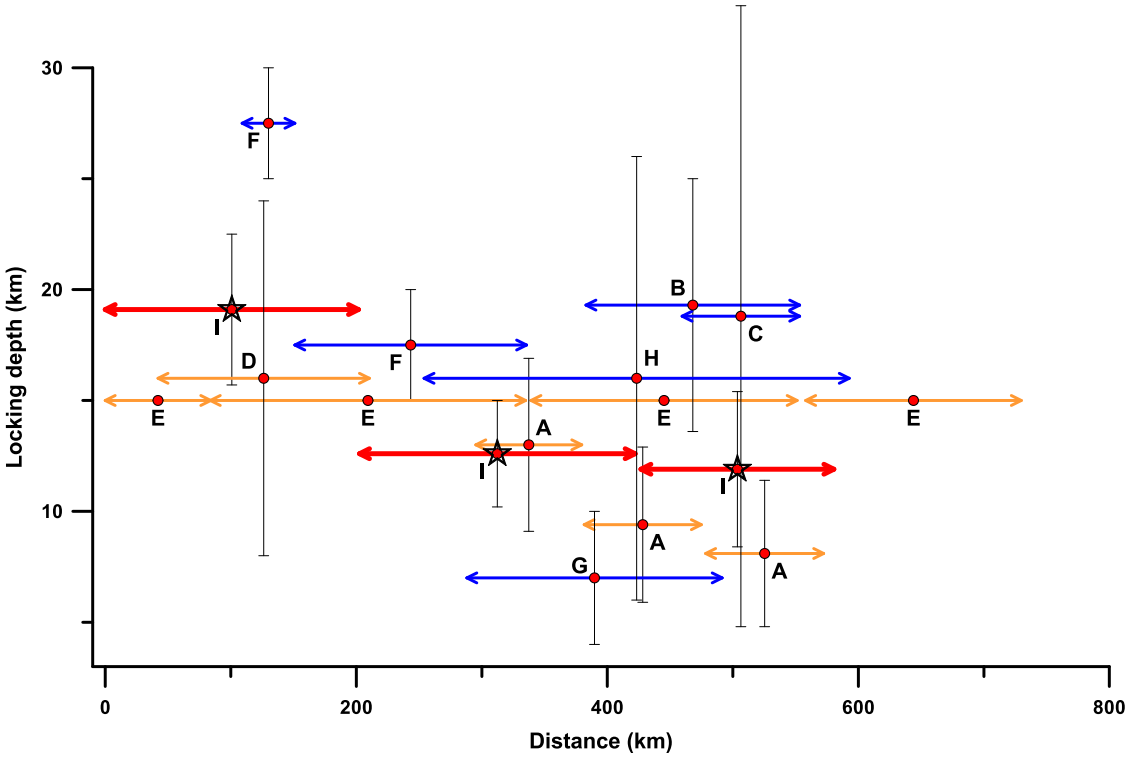

Figure 12. The variation of the locking depth along the eastern part of NAFS and the given uncertainties. The values are shown in red dots while the estimated values in this study are shown with an asterisk. The *x*-axis shows the distance from west to east and starts at 33° longitude. The uncertainties are shown at 1σ level. The estimates from GPS and InSAR are shown in orange and blue lines, respectively. The estimates in this study are shown in red lines. (A) Tatar *et al.* (2012); (B) Walters *et al.* (2011); (C) Wright *et al.* (2001); (D) Yavaşoğlu *et al.* (2011); (E) Reilinger *et al.* (2006); (F) Peyret *et al.* (2013); (G) Cakir *et al.* (2014); (H) Walters *et al.* (2014); (I) this study.

1254–1668, close to the stress drops of these earthquakes estimated from surface slip distributions (Barka 1996). The slower or more rapid accumulation of strain could also determine the earthquake recurrence intervals across different segments of the NAFS. In a time-predictable recurrence model, the relatively larger strain rates coupled with relatively shallower locking depth in the easternmost segment of the NAFS may imply a more frequent but smaller size earthquakes.

No asymmetry was observed within the studied segments of the NAFS as revealed by the very small and insignificant fault offsets. However, such an asymmetry could be valid for the westernmost segments of the NAFS as proposed by Le Pichon *et al.* (2005).

The analysis of the profiles shows that eastern part of the NAFS has a highly linear and vertical structure despite the geological complexities. Considering that the NAFS initiated in the east and propagated westwards (Şengör *et al.* 2005), such linearity could be associated with the relative maturity of the NAFS in the east.

ACKNOWLEDGEMENTS

We are grateful to the many individuals and institutions supporting the collection of data presented here. UNAVCO is particularly acknowledged for the data archive. We thank the editor and three anonymous reviewers for their reviews that helped to improve the manuscript. Some part of this work was completed during the sabbatical leave of the first author at Université Montpellier-II which was supported under the grant B.14.2.TBT.0.06.01-219-84 of The Scientific and Technological Research Council of Turkey (TUBITAK).

REFERENCES

Aktuğ, B. *et al.*, 2009a. Deformation of western Turkey from a combination of permanent and campaign GPS data: limits to block-like behaviour, *J. geophys. Res.*, **114,** B10404, doi:10.1029/2008JB006000.

Aktuğ, B., Lenk, O., Gürdal, M.A. & Kilicoglu, A., 2009b. Establishment Of Regional Reference Frames For Detecting Active Deformation Areas in Anatolia, *Stud. Geophys. Geod.,* **2**(53), 169–183.

Aktuğ, B., Parmaksız, E., Kurt, M., Lenk, O., Kılıçoğlu, A., Gürdal, M.A. & Özdemir, S., 2013a. Deformation of Central Anatolia: GPS Implications, *J. Geodyn.,* **67,** 78–96.

Aktuğ, B., Dikmen, Ü., Doğru, A. & Özener, H., 2013b. Slip rates near Karliova Triple Junction by GPS observations, *J. Geodyn.,* **67,** 21–29.

Ambraseys, N.N., 1970. Some characteristic features of the Anatolian fault zone, *Tectonophysics,* **9,** 143–165.

Ambraseys, N.N. & Finkel, C.F., 1988. The Anatolian earthquake of 17 August 1668, in *Proc. Symposium on Historical Seismograms and Earthquakes of the World,* pp. 173–180, eds Lee, W.H.K., Meyers, H. & Shimazaki, K., Academic Press.

Barka, A., 1996. Slip distribution along the North Anatolian fault associated with large earthquakes of the period 1939 to 1967, *Bull. seism. Soc. Am.,* **86,** 1238–1254.

Barka, A.A. & Kadinsky-Cade, K., 1988. Strike-slip fault geometry in Turkey and its influence on earthquake activity, *Tectonophysics,* **7,** 663–684.

Bozkurt, E., 2001. Neotectonics of Turkey—A synthesis, *Geodin. Acta,* **14,** 3–30.

Cakir, Z., Ergintav, S., Ozener, H., Dogan, U., Akoglu, A., Meghraoui, M. & Reilinger, R., 2012. Onset of aseismic creep on major strike slip faults, *Geology,* **40**(12), 1115–1118.

Cakir, Z., Ergintav, S., Akoğlu, A.M., Cakmak, R., Tatar, O. & Meghraoui, M., 2014. InSAR velocity field across the North Anatolian Fault

(E. Turkey): implications for the loading and release of interseismic strain accumulation, *J. geophys. Res.,* **119,** 7934–7943.

Cambaz, M.D. & Karabulut, H., 2010. Love Wave Group Velocity Maps of Turkey and Surrounding regions, *Geophys. J. Int.,* **181,** 502–520.

Chéry, J., 2008. Geodetic strain across the San Andreas fault reflects elastic plate thickness variations (rather than fault slip rate), *Earth planet. Sci. Lett.,* **269,** 351–364.

Dewey, J.F. & Sengör, A.M.C., 1979. Aegean and surrounding regions: complex multiplate and continuum tectonics in a convergent zone, *Bull. geol. Soc. Am*., **90,** 84–92.

Dong, D., Herring, T.A. & King, R.W., 1998. Estimating Regional Deformation from a combination of space and terrestrial geodetic data, *J. Geod.,* **72,** 200–214.

Erturaç, M.K. & Tuysuz, O., 2012. Kinematics and basin formation along the Ezinepazar-Sungurlu fault zone, NE Anatolia, Turkey, *Turk. J. Earth Sci.,* **21**(4), 497–520.

Fialko, Y., 2006. Interseismic strain accumulation and the earthquake potential on the southern San Andreas fault system, *Nature,* **441,** 968–971.

GCM, 2013. The velocity field of Turkish National Permanent GPS Network-Active, http://www.hgk.msb.gov.tr/

Hartleb, R.D., Dolan, J.F., Akyüz, H.S. & Yerli, B., 2003. A 2,000 year-long paleoseismologic record of earthquakes along the central North Anatolian fault, from trenches at Alayurt, Turkey, *Bull. seism. Soc. Am.,* **93,** 1935–1954.

He, J., Vernant, P., Chéry, J., Wang, W., Lu, S., Ku, W., Xia, W. & Bilhan, R., 2013. Nailing down the slip rate of the Altyn Tagh fault, *Geophys. Res. Lett.,* **40,** 5382–5386.

Hearn, E.H., McClusky, S., Ergintav, S. & Reilinger, R.E., 2009. Izmit earthquake postseismic deformation and dynamics of the North Anatolian Fault Zone, *J. Geophys. Res.,* **114,** B08405, doi:10.1029/2008JB006026.

Herece, E. & Akay, E., 2003. Kuzey Anadolu Fayı (KAF) Atlası/Atlas of North Anatolian Fault (NAF). Maden Tetk. Arama Genel Müdürlüğü Özel Yayın. Ser. 2, Ankara, [IV]+61 pp.+13 appendices as separate maps.

Herring, T., 2003. MATLAB Tools for viewing GPS velocities and time series, *GPS Solutions,* **7**(3), 194–199.

Hubert-Ferrari, A., Armijo, R., King, G., Meyer, B. & Barka, A.A., 2002. Morphology, displacement, and slip rates along the North Anatolian fault, Turkey, *J. geophys. Res.,* **107,** 2235, doi:10.1029/2001JB000393.

Jackson, J.A. & McKenzie, D.P., 1984. Active tectonics of Alpine-Himalayan Belt between western Turkey and Pakistan, *Geophys. J. R. astr. Soc.,* **77,** 185–265.

Jolivet, R., Cattin, R., Chamot-Rooke, N., Lasserre, C. & Peltzer, G. 2008. Thin-plate modeling of interseismic deformation and asymmetry across the Altyn Tagh fault zone, *Geophys. Res. Lett.,* **35,** L02309, doi:10.1029/2007GL031511.

Kalafat, D., Kekovali, K., Günes, Y., Yilmazer, M., Kara, M., Deniz, P & Berberoglu, M., 2009. *A Catalogue of Source Parameters of Moderate and Strong Earthquakes for Turkey and its Surrounding Area (1938–2008),* Bogaziçi University Publication.

Kalafat, D., Güneş, Y., Kekovalı, K., Kara, M, Deniz, P. & Yılmazer, M., 2011. *A Revised and Extented Earthquake Cataloque for Turkey since 1900 (1900–2010; M > 4.0),* Bogaziçi University Publication.

Kaneko, Y., Fialko, Y., Sandwell, D.T., Tong, X. & Furuya, M., 2013. Interseismic deformation and creep along the central section of the North Anatolian fault (Turkey): InSAR observations and implications for rate-and-state friction properties, *J. geophys. Res.,* **118,** 1–15.

King, R.W., McClusky, S. & Herring, T., 2009. *Documentation of the GAMIT GPS Analysis Software, Release 10.3*, Massachusetts Institute of Technology.

Koçbulut, F., Kavak, K.Ş. & Tatar, O., 2014. Analysis of Ezinepazarı-Sungurlu Fault Zone (Turkey) using Landsat TM data and its kinematic implications, *Arab. J. Geosci.,* 1–15, doi:10.1007/s12517-014-1660-z.

Kozacı, Ö., Dolan, J.F., Finkel, R.C. & Hartleb, R.D., 2007. Late Holocene slip rate for the North Anatolian fault, Turkey, from cosmogenic 36Cl geochronology: Implications for the constancy of fault loading and strain release rates, *Geology,* **35**(10), 867–870.

Kozacı, Ö., Dolan, J.F. & Finkel, R.C., 2009. A late Holocene slip rate for the central North Anatolian fault, at Tahtakopru, Turkey, from cosmogenic ^{10}Be geochronology: implications for fault loading and strain release rates, *J. geophys. Res.,* **114,** B01405, doi:10.1029/2008JB005760.

Kozacı, Ö., Dolan, J., Yönlü, Ö. & Hartleb, R.D., 2011. Paleoseismologic evidence for the relatively regular recurrence of infrequent, large-magnitude earthquakes on the eastern North Anatolian fault at Yaylabeli, Turkey, *Lithosphere,* **3,** 37–54.

Lawson, C.L. & Hanson, R.J., 1995. *Solving Least Squares Problems*, SIAM.

Le Pichon, X. & Angelier, J., 1979. The Hellenic arc and trench system: a key to the neotectonic evolution of the eastern Mediterranean area, *Tectonophysics,* **60,** 1–42.

Le Pichon, X, Kreemer, C. & Chamot-Rooke, N., 2005. Asymmetry in elastic properties and the evolution of large continental strike-slip, *J. geophys. Res.,* **110,** B03405, doi:10.1029/2004JB003343.

Matsu'ura, M., Jackson, D.D. & Cheng, A. 1986. Dislocation model for aseismic crustal deformation at Hollister, California, *J. geophys. Res.,* **91**(B12), 2661–2674.

McCaffrey, R., 2002. Crustal block rotations and plate coupling, in *Plate Boundary Zones: Geodynamics Series,* Vol. 30, pp. 101–122, eds Stein, S. & Freymueller, J.T., American Geophysical Union.

McCaffrey, R., 2005. Block kinematics of the Pacific-North America plate boundary in the southwestern United States from inversion of GPS, seismological, and geologic data, *J. geophys. Res.,* **110**(B7), B07401, doi:10.1029/2004JB003307.

McClusky, S. *et al.*, 2000. Global positioning system constraints on plate kinematics and dynamics in the eastern Mediterranean and Caucasus, *J. geophys. Res.,* **105**(B3), 5695–5719.

Meade, B.J., Hager, B., McClusky, S.C., Reilinger, R.E., Ergintav, S., Lenk, O., Barka, A. & Özener, H., 2002. Estimates of seismic potential in the Marmara Sea region from block models of secular deformation constrained by GPS measurements, *Bull. seism. Soc. Am.,* **92,** 208–215.

Meghraoui, M., Aksoy, M.E., Akyüz, H.S., Ferry, M., Dikbaş, A. & Altunel, E., 2012. Paleoseismology of the North Anatolian Fault at Güzelköy (Ganos segment, Turkey): size and recurrence time of earthquake ruptures west of the Sea of Marmara, *Geochem. Geophys. Geosyst.,* **13,** Q04005, doi:10.1029/2011GC003960.

Nocquet, J.-M., 2012. Present-day kinematics of the Mediterranean: a comprehensive overview of GPS results, *Tectonophysics,* **579,** 220–242.

Okay, A.I. & Tüysüz, O., 1999. Tethyan sutures of northern Turkey, in *The Mediterranean Basins: Tertiary Extension within the Alpine Orogen,* Vol. 156, pp. 475–515, eds Durand, B., Jolivet, L., Horváth, F. & Séranne, M., Geological Society, London, Special Publications.

Okada, Y., 1985. Surface deformation due shear and tensile faults in a halfspace, *Bull. seism. Soc. Am.,* **75,** 1135–1154.

Oral, M.B., Reilinger, R.E., Toksöz, M.N., King, R.W., Barka, A.A., Kınık, I. & Lenk, O., 1995. Global positioning system offers evidence of plate motions in eastern Mediterranean, *EOS, Trans. Am. geophys. Un.,* **76**(9), 9–11.

Özener, H., Arpat, E., Ergintav, S., Dogru, A., Cakmak, R., Turgut, B. & Dogan, U., 2010. Kinematics of the Eastern Part of the North Anatolian Fault Zone, *J. Geodyn.,* **49**(3–4), 141–150.

Özener, H., Doğru, A. & Turgut, B., 2013. Quantifying aseismic creep on the Ismetpasa segment of the North Anatolian Fault Zone (Turkey) by 6 years of GPS observations, *J. Geodyn.,* **67,** 72–77.

Peyret, M., Masson, F., Yavasoğlu, H., Ergintav, S. & Reilinger, R., 2013. Present-day strain distribution across a segment of the central bend of the North Anatolian Fault Zone from a Persistent-Scatterers InSAR analysis of the ERS and Envisat archives, *Geophys. J. Int.,* **192,** 929–945.

Reilinger, R. *et al.*, 2006. GPS constraints on continental deformation in the Africa-Arabia-Eurasia continental collision zone and implications for the dynamics of plate interactions, *J. geophys. Res.,* **111,** B05411, doi:10.1029/2005JB004051.

Reilinger, R.E., McClusky, S., Oral, M.B., King, W. & Toksöz, M.N., 1997. Global positioning, system measurements of present-day crustal movements in the Arabian–Africa–Eurasia plate collision zone, *J. geophys. Res.,* **102,** 9983–9999.

Şaroğlu, F., Emre, Ö. & Kuş, İ., 1992. *Turkish Active Faults Map,* Directoriate of Mineral Research and Exploration.

Savage, J.C. & Burford, R.O., 1973. Geodetic determination of relative plate motion in Central California, *J. geophys. Res.,* **78,** 832–845.

Scholz, C., 1998. Earthquakes and friction laws, *Science,* **391,** 37–42.

Seber, G.A.F. & Wild, C.J., 2003. *Nonlinear Regression,* Wiley-Interscience.

Segall, P., 2010. *Earthquake and Volcano Deformation,* Princeton University Press, 464 pp.

Şengör, A.M.C., Tüysüz, O., İmren, C., Sakınç, M., Eyidoğan, H., Görür, N., Le Pichon, X. & Rangin, C.C., 2005. The North Anatolian fault: a new look, *Annual Review of Earth and Planetary Sciences,* **33,** 1–75.

Stein, R.S., Barka, A.A. & Dieterich, J.H., 1997. Progressive failure on the North Anatolian fault since 1939 by earthquake stress triggering, *Geophys. J. Int.,* **128,** 594–604.

Straub, C., Kahle, H.G. & Schindler, C., 1997. GPS and geologic estimates of the tectonic activity in the Marmara Sea region, NW Anatolia, *J. geophys. Res.,* **102**(B12), 27 587–27 601.

Tatar, O., Piper, J.D.A., Graham, P.R. & Gürsoy, H., 1995. Palaeomagnetic study of block rotations in the Niksar overlap region of the North Anatolian Fault Zone, central Turkey, *Tectonophysics,* **244,** 251–266.

Tatar, O. *et al.*, 2012. Crustal deformation and kinematics of the eastern part of the North Anatolian fault zone (Turkey) from GPS measurements, *Tectonophysics,* **518–521,** 55–62.

Walters, R.J., Holley, R.J., Parsons, B.E. & Wright, T.J., 2011. Interseismic strain accumulation across the North Anatolian Fault from Envisat InSAR measurements, *Geophys. Res. Lett.,* **38,** L05303, doi: 10.1029/2010GL046443.

Walters, R.J., Parsons, B. & Wright, T.J., 2014. Constraining crustal velocity fields with InSAR for Eastern Turkey: limits to the block-like behavior of Eastern Anatolia, *J. geophys. Res.,* **119,** 5215–5234.

Wang, L., Wang, R., Roth, F., Enescu, B., Hainzl, S. & Ergintav, S., 2009. Afterslip and viscoelastic relaxation following the 1999 *M* 7.4 Izmit earthquake from GPS measurements, *Geophys. J. Int.,* **178**(3), 1220–1237.

Wright, T.J., Parsons, B.E. & Fielding, E.J., 2001. Measurement of interseismic strain accumulation across the North Anatolian Fault by satellite radar interferometry, *Geophys. Res. Lett.,* **28,** 2117–2120.

Yavaşoğlu, H., Tarı, E., Tüysüz, O., Çakır, Z. & Ergintav, S., 2011. Determining and modeling tectonic movements along the central part of the North Anatolian Fault (Turkey) using geodetic measurements, *J. Geodyn.,* **51,** 339–343.

Zabci, C., Akyüz, H.S., Karabacak, V., Sançar, T., Altunel, E., Gürsoy, H. & Tatar, O., 2011. Palaeoearthquakes on the Kelkit Valley segment of the North Anatolian Fault, Turkey: implications for the surface rupture of the historical 17 August 1668 Anatolian earthquake, *Turk. J. Earth Sci.,* **20**(4), 411–427.